SOME STUDIES ON THE GEOMETRIC PARAMETERS OF THE STRAIGHT PARALLEL FLOW FIELD DESIGN OF PROTON EXCHANGE MEMBRANE FUEL CELL

A DISSERTATION

SUBMITTED IN PARTIAL FULFILLMENT OF THE REQUIREMENTS FOR THE AWARD OF THE DEGREE OF

MASTER OF TECHNOLOGY

IN

THERMAL ENGINEERING

Submitted by:

SUBHASH DWIVEDI

(2K21/THE/16)

Under the supervision of

DR. NAVEEN KUMAR

(PROFESSOR)

DEPARTMENT OF MECHANICAL ENGINEERING

DELHI TECHNOLOGICAL UNIVERSITY

(Formerly Delhi College of Engineering)

Bawana Road, Delhi-110042

MAY, 2023

MECHANICAL ENGINEERING DEPARTMENT

DELHI TECHNOLOGICAL UNIVERSITY

(Formerly Delhi College of Engineering)

Bawana Road, Delhi – 110042

CANDIDATE'S DECLARATION

I, **SUBHASH DWIVEDI, 2K21/THE/16**, of M. Tech (Thermal Engineering), hereby, declare that the project Dissertation titled "**Some Studies on the Geometric Parameters of the Straight Parallel Flow Field Design of Proton Exchange Membrane Fuel Cell**" which is submitted by me to the Department of Mechanical Engineering, Delhi Technological University, Delhi in partial fulfilment of the requirement for the award of the degree of Master of Technology, is original and not copied from any source without proper citation. This work has not previously formed the basis for the award of any Degree, Diploma Associateship, Fellowship, or other similar title or recognition.

Place: Delhi   **SUBHASH DWIVEDI**

Date:

CERTIFICATE

I hereby certify that the Project Dissertation titled "**Some Studies on the Geometric Parameters of the Straight Parallel Flow Field Design of Proton Exchange Membrane Fuel Cell**" which is submitted by **SUBHASH DWIVEDI, 2K21/THE/16**, Department of Mechanical Engineering, Delhi Technological University, Delhi in partial fulfilment of the requirement for the award of the degree of Master of Technology, is a record of the project work carried out by the student under my supervision. To the best of my knowledge, this work has not been submitted in part or full for any Degree or Diploma to this University or elsewhere.

Place: Delhi

Date:

DR. NAVEEN KUMAR

SUPERVISOR

Professor, Department of Mechanical Engineering

Delhi Technological University

Bawana road, Delhi – 110042

ACKNOWLEDGEMENT

I would like to offer my heartfelt appreciation to everyone who helped me finish this academic project. This initiative would not have been feasible without their assistance and support.

First and foremost, I would want to thank **Dr. Naveen Kumar** (Professor, Delhi Technological University), my academic project supervisor, for leading me through the project and giving me vital insights and criticism. I appreciate the time and work he has put into me.

I would like to thank **Prof. S.K Garg** (Head of the Department, Delhi technological university) and my teachers for motivating and inspiring me throughout this journey, and for their brilliant comments and suggestions.

I also want to thank my family and friends for their constant support and encouragement during this effort. Their faith in me has been both motivating and inspiring.

Finally, I'd want to thank God for allowing me to go through all of this. Day by day, I've felt your leadership. You are the one who allowed me to complete my degree. I will continue to put my faith in you for my future.

SUBHASH DWIVEDI

ABSTRACT

In an era where environmental concerns have reached a critical point, the quest for clean and efficient energy sources has become paramount. Proton exchange membrane fuel cells (PEMFCs) offer a glimmer of hope, with their ability to directly convert the chemical energy of fuels into useful work, leaving a negligible environmental impact. However, maximizing the performance of PEMFCs requires innovative design approaches, particularly in the realm of flow field Designs (FFDs) of the bipolar plates (BPs).

The study presents a comprehensive analysis of the performance and local species transport phenomena of PEMFCs, focusing on the impact of geometric designs and FFDs. An enhanced FFD provides more homogeneous reactant diffusion in the cell, lowers the pressure drop, and provides higher electrical performance. The FFDs can be improved by adding baffles in the flow channel, developing completely new and innovative FFDs, or adopting nature/bio-inspired designs. However, a detailed analysis of various aspects of FFDs like cell performance, cost, and manufacturing difficulties has to be done

Therefore, a simple and novel tapered-trapezoidal FFD is proposed considering the varying dimensions of the parallel sides at the inlet, denoted as "a" and "b", aiming to enhance the performance of PEMFCs compared to conventional straight parallel FFD and tapered FFD. For this purpose, a three-dimensional non-isothermal, single-phase, steady-state, model for a single PEMFC is developed. The equations governing the transfer of

mass and momentum are carefully solved by the ANSYS program using the computational fluid dynamics (CFD) technique, taking into account the relevant source terms arising from electrochemical reactions occurring in various zones of the fuel cell.

The study revealed that the geometrical dimensions of the FFDs had a substantial impact on the electrochemical reactions and electrical characteristics of the cell. Compared with the conventional straight parallel FFD and tapered FFD, the proposed novel tapered-trapezoidal FFD enhances the temperature distributions, reactants distributions, water removal, and cell performance. According to the results, the limiting current density and maximum power density of the proposed novel tapered-trapezoidal FFD with case C4 have 13.8 % and 8.1 % with respect to the conventional straight parallel FFD respectively, and 7.9 % and 4.3 % with respect to the tapered FFD at 0.5 V. Moreover, an increase in the maximum temperature of the novel FFDs compared to C1 and C2 results in improved heat transfer efficiency of the PEMFC. The average oxygen mass fraction at the interface between the channel and GDL on the cathode side for case C4 is 19.8 % more than C1. In addition, the water removal capability has also improved for the novel tapered-trapezoidal FFDs. Therefore, the employment of the proposed design can be strongly recommended for high current-density operating conditions. The present study discusses in detail the reasoning for the mentioned observations.

CONTENTS

LIST OF TABLES

LIST OF FIGURES

LIST OF SYMBOLS AND ABBREVIATIONS

Abbreviations	
IEA	International Energy Agency
UNFCCC	United Nations Framework Convention on Climate Change
COP	Conference of the Parties
EJ	Exajoule
bcm	Billion cubic meters
MTPA	Million tonnes per annum
FC	Fuel cell
PEMFC	Proton exchange membrane fuel cell
CFD	Computational fluid dynamics
FVM	Finite volume method
MEA	Membrane electrode assembly
CL	Catalyst layer
GDL	Gas diffusion layer
FFD	Flow field design
BPP	Bipolar plate
PEM	Proton exchange membrane
PSFF	Parallel serpentine flow field
PSBFF	Parallel serpentine-baffled flow field
MSTV	Multi-stage Tesla valve
OCV	Open circuit voltage
EMF	Electromotive force
CH	Channel
ppm	Part per million
CO_2	Carbon dioxide
GHG	Greenhouse gas
H_2	Hydrogen
O_2	Oxygen

a_w	Water activity
c_p	Specific heat capacity, $J kg^{-1} K^{-1}$
D	Diffusion coefficient, $m^2 s^{-1}$
D_w	Water diffusivity, $m^2 s^{-1}$
E_o	Reversible potential, V
F	Faraday constant, 96,485 $C\ mol^{-1}$
h	Enthalpy, $kJ\ kg^{-1} K^{-1}$
I	Current, A
J	Transfer current density, $A\ m^{-3}$
K	Thermal conductivity, $W\ m^{-1}\ K^{-1}$
K_p	Permeability, m^2
M	Molecular weight, $kg\ kmol^{-1}$
$M_{m,dry}$	Equivalent weight of a dry membrane, $kg\ kmol^{-1}$
η_d	Electro-osmotic drag coefficient
P	Pressure, Pa
T	Temperature, K
u	Velocity $m\ s^{-1}$
V	Voltage
X	Mole fraction
Y	Mass fraction
R	Universal gas constant, 8.314 $kJ\ kmol^{-1}\ K^{-1}$
S	Source term
C	Molar concentration, $kmol\ m^{-3}$
Greek letters	
$\underline{\alpha}$	Transfer coefficient
Υ	Concentration dependence
ε	Porosity
η	Overpotential, V
λ	Water content
μ	Viscosity, $kg\ m^{-1}\ s^{-1}$
ζ	Specific active surface area, m^{-1}
ρ	Density, $kg\ m^{-3}$
$P_{m,dry}$	Density of dry membrane, $kg\ m^{-3}$

σ	Electrical conductivity, Ω^{-1} m^{-1}
φ	Phase potential, V
Subscript	
an	anode
ca	cathode
i	Gas species
mem	Electrolyte phase
ohm	Ohmic
react	Reaction
ref	reference
sat	saturated
sol	
Superscript	
eff	effective
ref	Reference

CHAPTER 1

INTRODUCTION

1.1 ENERGY CRISIS

The energy crisis emerges as one of the top ten global threats, ranking fourth, alongside rising fuel costs, disruptions in supply chains, global expansion, and the effects of Russia's involvement in Ukraine [1]. The world is currently experiencing an unprecedented "truly global energy crisis," according to the International Energy Agency (IEA). This crisis not only puts millions of people in difficult situations but also has the potential to benefit them in the long run [2]. The intergovernmental organization's Renewables 2022 report says that since Russia invaded Ukraine in February, there has been a significant increase in the expansion of green energy capacity. The report features that worldwide renewable capacity growth is projected to almost twofold throughout the following five years, outperforming coal as the essential supporter of the power age [3]. "Renewable energy sources were already experiencing rapid expansion, but the current global energy crisis has propelled them into an exceptional new stage of accelerated development as nations strive to leverage their advantages in energy security," says IEA Executive Director Fatih Birol. The current energy crisis is a significant turning point that has the potential to prompt a paradigm shift in favor of a more secure and environmentally friendly energy system. In order to preserve the potential of achieving the objective of capping global warming at 1.5 degrees Celsius, renewable energy sources must continue to advance at a rapid pace [4].

1.2 ENERGY SCENARIO

Energy has shifted from being a broad technological field to a crucial aspect of economic planning and international relations. It serves as the bedrock for the socio-economic development of any nation. In a country like India where 80% of demand is still being met by fossil fuels. Energy is a very crucial entity for its economic as well as social developments. India has established its rank as the third-largest energy consumer in the world as a result of increasing incomes and improved living standards. India's per capita energy usage and emissions are below half of the worldwide average, along with

other significant indicators such as vehicle ownership, steel production, and cement output. [5]. India had an improvement in its primary energy consumption in 2021, surpassing its pre-pandemic level in 2019 by 3.7%, after recovering from the economic crisis brought on by the Covid-19 pandemic. All other fuels had a spike in usage during the same time period, with the exception of nuclear and hydropower.[6]. Table 1.1 depicts the breakdown of primary energy in India.

Table 1.1. Breakdown of Primary Energy in India [6]

Consumption	Year wise Distribution			Growth rate per year in %	
	2010	2020	2021	2010-20	2021
Primary energy	23	32	35	3.6	10
Oil	6.6	9.1	9.4	3.2	3.9
Natural Gas	2.1	2.2	2.2	0.2	3.1
Coal	12	17	20	3.6	16
Nuclear	0.2	0.4	0.4	6.2	-1.6
Hydro	1.1	1.5	1.5	3.6	-2.2
Renewable	0.4	1.6	1.8	14.7	13.2
• Units in EJ unless otherwise stated					

Oil, gas, and coal together comprised 90% of the energy consumed, maintaining a level similar to before the pandemic. Notably, coal exhibited the highest growth rate among these fuels, with a 16% increase and surpassing its 2019 level by 8%. Coal's share in primary energy reached 57%, in contrast to the global average of 24%. It is worth mentioning that India, as the second-largest coal producer in the world, (after China), accounts for 12.5% of global coal consumption.[6]. Natural gas, a versatile and abundant fossil fuel, plays a crucial role in powering various sectors of Indian economic activities such as transportation as well as electricity. India's natural gas production increased by 20%, hitting 29 billion cubic metres (bcm), nevertheless, it is still below the peak of 47 bcm seen in 2010. In contrast, imports of liquefied natural gas (LNG) fell by 8.1% to 33.6 bcm. Qatar had the largest proportion (41%) of the nation's supplying LNG to India [6].
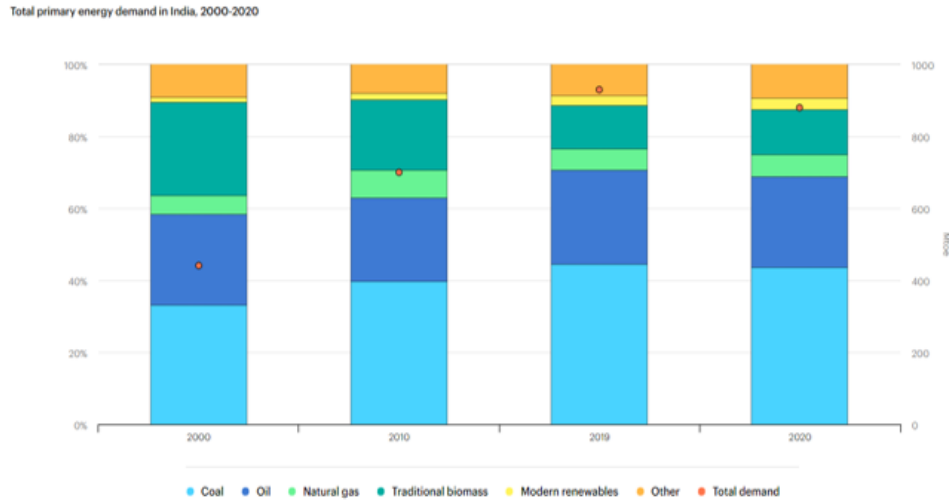
Figure 1.1: India's Overall Primary Energy Demand 2000-2020 [5]

1.3 RENEWABLE ENERGY SOURCES

India is rapidly transforming its power generation mix towards a greater percentage of renewable energy in line with the goals of sustainable development. India ranks fourth globally in terms of its installed renewable energy capacity, which includes large hydroelectric power projects. According to the REN21 Renewables 2022 Global Status Report, its wind and solar power capacity places it in fourth place. India set a lofty goal to produce 500 GW of clean energy by the year 2030 during the COP26 summit. As of February 2023, the total installed capacity of large hydropower and other renewable energy sources stands at 178.79 GW as depicted in Table 1.2 [7]:

Table 1.2. India's Installed Capacity for Renewable Energy [7]

India's installed capacity for renewable energy in GW					
Solar	Wind	Large Hydro	Small Hydro	Biomass	Waste to Energy
66.7	42.6	46.85	4.94	10.2	0.55

India's installed non-fossil fuel capacity has grown by an astonishing 396% during the past 8.5 years, achieving a historic milestone of over 178.79 gigawatts (GW), including huge hydro. As of May 2023, this represents over 43% of the nation's entire capacity. In 2022, India achieved the highest year-on-year growth in renewable energy additions, with a notable increase of 9.83%. As of May 2023, the installed solar energy capacity had increased by a noteworthy 24.4 times during the previous nine years, reaching 66.7 GW. The installed renewable energy capacity, which includes large hydro, has seen a significant increase of about 128% since 2014 [7]. With ambitious

targets and continued efforts India's renewable energy share is continuously increasing as shown in Figure 1.2, resulting in more economic independence and developments of more sustainable technologies like electrolyzers and fuel cells which helped India to achieve its net zero carbon emission by the year 2070. Figure 1.2 depicts the power generation from renewable energy sources in India from 1997.
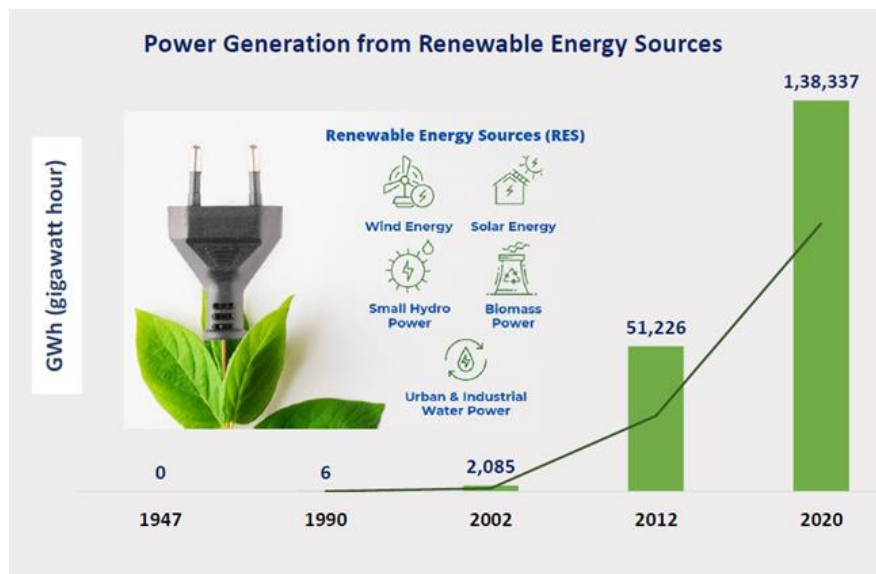
Figure 1.2: Power Generation from Renewable Energy Sources [8]

1.4 THE FUTURE OUTLOOK

Before the worldwide pandemic, the anticipated growth in India's energy demand was nearly 50% from 2019 to 2030. However, in the STEPS (Stated Policies Scenario) and the "Delayed Recovery Scenario," the expected growth during this time has been lowered to around 35% and 25%, respectively [5]. According to the IEA's World Energy Outlook 2021, India currently accounts for 6.1% of the world's primary energy usage, and under the scenario of the stated policies, the figure is expected to grow to almost 9.8% by 2050 [2]. According to the BPSR research, throughout a 40-year period, coal's share of total primary energy has stayed largely constant at 45% since 2019. However, the share of coal decreases and is anticipated to vary from 6% to 33% by 2050 in all three scenarios (Accelerated, Net Zero, and New Momentum). On the other hand, demand from the industrial and heavy road transport sectors drives an increase in natural gas's share of total primary energy across all scenarios, from 5% in 2019 to 7-11% in 2050 [6]. Renewable energy grows strongly in all scenarios, at an average of 4-6% a year. As a result, in the Accelerated and Net Zero scenarios as well as the New Momentum scenario, renewable energy surpasses coal as the dominant

energy source in 2050. Electricity generation in 2050 is around four times that in 2019 in New Momentum and Accelerated, and five times in Net Zero, with solar and wind power providing 57% to 95% of that growth. Solar and wind installed capacities in 2050 reach 1.3-2.2 TW and 0.3-1.2TW, respectively, depending on the scenarios. Hydrogen demand grows by a factor of four in New Momentum up to a twelve-fold increase in Net Zero.
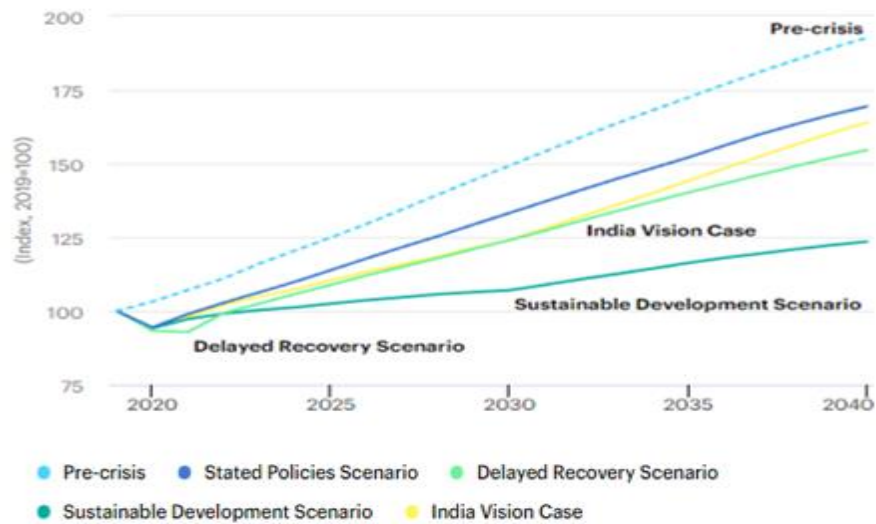
Figure 1.3 By Scenario, Energy Demand in India 2019-2040 [9]

In 2050 green hydrogen represents 47% of total production in New Momentum and 80% in Net Zero [6]. The goal for India is to produce 5 million tonnes of renewable hydrogen by 2030. This will be supported by 125 GW of renewable energy capacity. India has approved 57 solar parks, totaling a capacity of 39.28 GW. The offshore wind energy aim is 30 GW by 2030 [7]

1.5 DEGRADATION OF THE GLOBAL ENVIRONMENT

The uncontrolled and inefficient consumption of energy has led to environmental deterioration, necessitating thorough investigation. The generation, transportation, and usage of energy produce air pollutants. The ineffective utilization of energy has strained the Earth's ecosystems, as evident from the extraordinary and negative natural events witnessed in recent years. Examples of these consequences include the greenhouse effect, climate change, acid rain, air pollution, deforestation, and alterations in weather patterns. The escalating severity of these issues highlights the urgent need to study and address the environmental impacts of energy usage. The atmospheric concentration of carbon dioxide plays a role in both global warming and

the ensuing climate change. The atmospheric concentration of carbon dioxide has increased by 50% over a period of less than two centuries due to human activity. The data presented in Figure 1.4 depicts recent observations of CO_2 concentrations in the atmosphere at the Mauna Loa Observatory in Hawaii., ignoring seasonal and natural changes. The CO_2 content has climbed from 365 ppm in 2002 to more than 400 ppm at this time. These measurements are based on data from the mid-troposphere, which is the atmospheric layer that is located between 8 and 12 kilometres above the surface of the Earth [10].
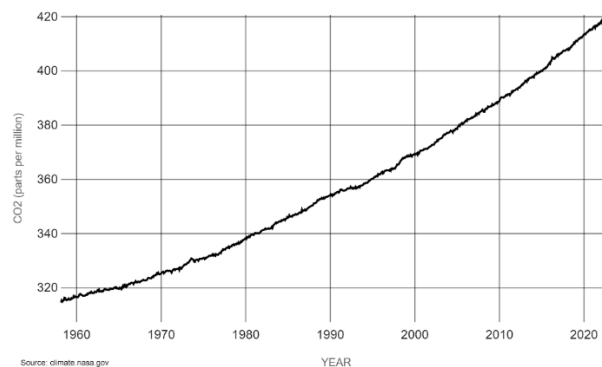
Figure 1.4: CO₂ Measurements:1958-Present [10]

Figure 1.5 depicts the variations in CO_2 levels throughout the Earth's previous three glacial cycles. Since the 18th century, when the industrial period began, human actions have led to a 50% increase in atmospheric CO_2, resulting in the current concentration being 150% of its value in 1750. This rise surpasses the natural changes that occurred about 20,000 years ago, near the end of the last ice age.
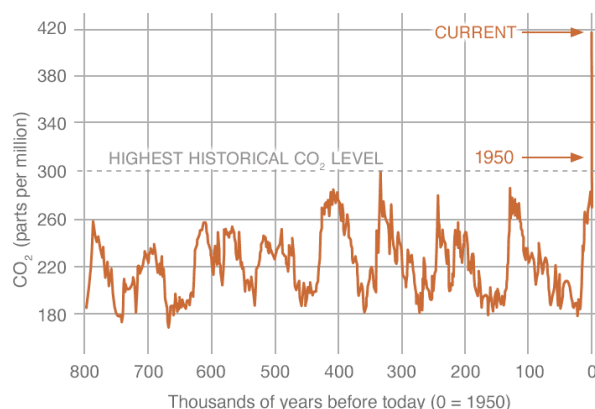
Figure 1.5: CO₂ Concentrations During the Previous Three Glacial Cycles on Earth [10]

Therefore, human activities are amplifying the naturally occurring greenhouse effect and raising global temperatures by increasing the concentration of CO_2 in the

atmosphere. According to the NOAA Global Monitoring Lab, CO_2 constituted approximately two-thirds of the overall warming impact attributed to human-generated greenhouse gases in 2021 [10].

1.6 CO_2 EMISSION OUTLOOK

Global carbon dioxide emissions are predicted to increase from 35.3 billion metric tonnes in 2018 to roughly 43.08 billion metric tonnes by 2050 under a business-as-usual scenario as shown in Figure 1.6. 2018 witnessed the greatest level of carbon dioxide emissions recorded in history due to a strong economy and severe weather. Summer heat waves increase the need for air conditioning, and harsher winters raise the need for heating, which leads to increased CO_2 emissions in the future[11].
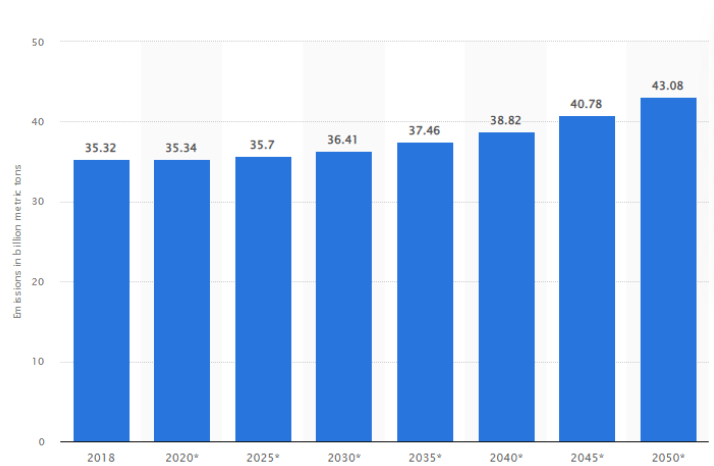
Figure 1.6: CO_2 Emissions worldwide from 2018 to 2050 [11]

Figure 1.7 illustrates the geographical distribution of global CO_2 emissions across different regions. Historically, until the early 20th century, Europe and the United States were the primary contributors to global emissions. In 1900, Europe and the US accounted for more than 90% of emissions, and even in 1950, they continued to make for more than 85% of emissions on an annual basis. But in recent years, there has been a noticeable change. In particular, Asia, with China being the most notable, saw a significant rise in emissions throughout the second half of the 20th century, followed by India. Currently, the US and Europe together contribute to less than one-third of global emissions. [12]. India's economy and population are both developing quickly, which has resulted in a large rise in emissions in recent years. It is now, after China and the United States, the world's third-largest emitter of greenhouse gases (GHGs). India contributed around 7% of the world's emissions in 2021, totaling 3.9 billion metric tonnes of carbon dioxide equivalent (GtCO2e). India's numbers are far lower than the global average

when per capita emissions are taken into account, coming in at just 2.8 tCO2e. In contrast, per-person emissions in China and the United States are 9.6 and 17.6 tCO2e, respectively. Additionally, India's historical cumulative CO_2 emissions, which total less than 4%, are much lower than those of other large economies[12].
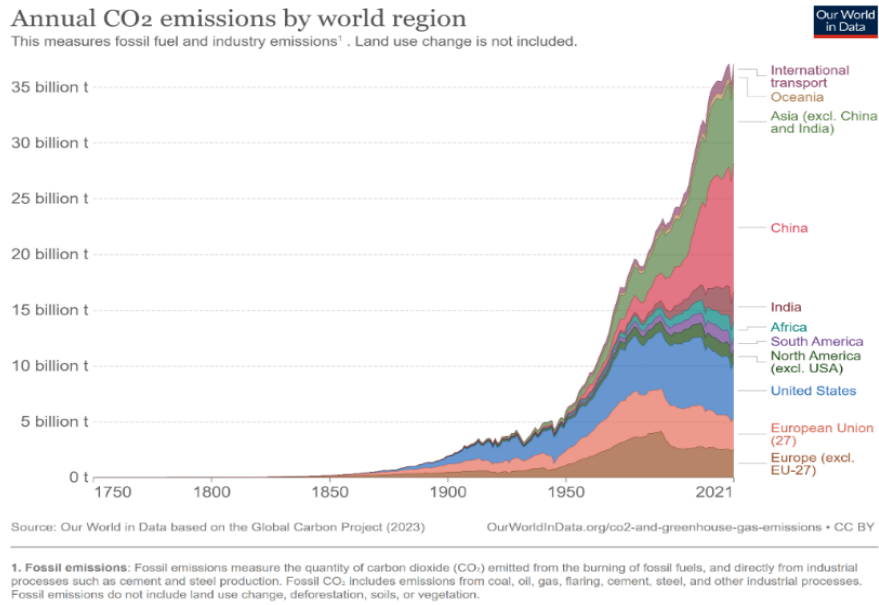
Figure 1.7: Annual CO2 Emission by the World Region [12]

Figure 1.8 displays the global and Indian CO_2 emissions by fuel or industry type. It is obvious that coal, which is followed by oil and then gas, has a major effect on CO_2 emissions worldwide as well as in India.
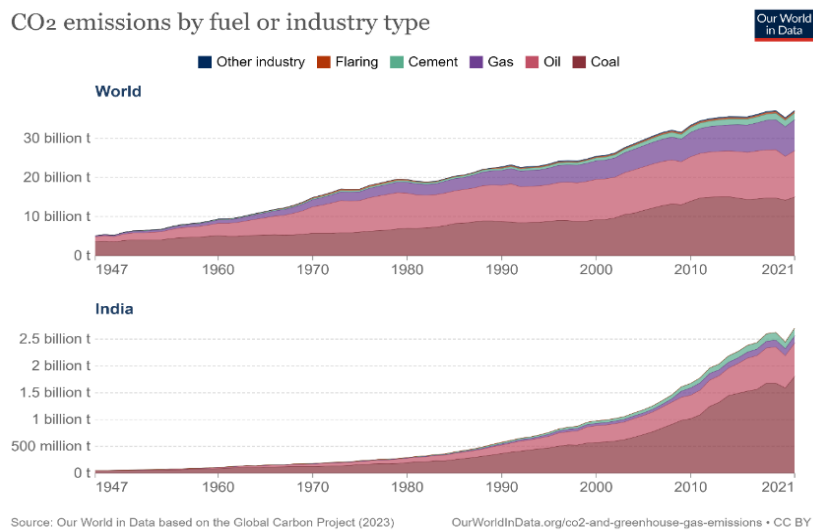
Figure 1.8: CO2 Emissions by the Fuel or Industry Type [12]

1.7 CLIMATE CHANGE

A region's predominant, long-term weather patterns are referred to as its climate. It encompasses various elements such as precipitation, temperature, humidity, sunshine, wind speed, and natural phenomena like fog, frost, and hailstorms. Climate change can be referred to the alterations in the climate over time, whether caused by natural variations or human actions. Climate change is defined as changes in the climate that can be directly or indirectly ascribed to anthropogenic activity in the UNFCCC reports. Along with the natural climate variations that have been seen over comparable time periods, these activities have an effect on the composition of the Earth's atmosphere. The atmosphere's rising greenhouse gas (GHG) content is the main factor in climate change. This accumulation of GHGs is promptly transforming the way atmosphere absorbs and retains energy. The main culprits among these gases are CO_2, released via the burning of fossil fuels; methane (CH_4) and nitrous oxide (N_2O), emitted from agricultural practices, land use changes, and other human activities; ozone ($O3$), primarily generated by vehicle emissions; and chlorofluorocarbons (CFCs) [13]. These greenhouse gases hinder the emission of infrared radiation from the Earth's atmosphere into outer space, leading to what is commonly referred to as "global warming.". Between the years 2030 and 2050, it is projected that climate change will lead to an extra 250,000 deaths each year, mainly caused by factors such as famine, malaria, diarrhea, and heat-induced strain. By 2030, it is predicted that these consequences will cost the healthcare industry somewhere between US$2 billion and US$4 billion annually. Without outside assistance for readiness and reaction, developing countries, especially those with weak healthcare facilities, will suffer the greatest difficulties in addressing these repercussions [14].

Mitigation and adaptation are the two primary pillars of climate change policy. The goal of mitigation is to lower greenhouse gas emissions through the use of renewable energy, environmentally friendly transportation, energy conservation, and carbon capture. Adaptation aims to reduce the repercussions of climate change through resilient infrastructure, improved water management, agricultural practices, early warning systems, and ecosystem preservation. Both pillars are crucial for addressing climate change and building a sustainable and resilient future.

1.7.1 Effect of Global Warming

Fossil fuels, which are also referred to as oil, gas, and coal, are the primary drivers of the global climate problem. Over 75% of all greenhouse gas emissions worldwide are attributed to them, with CO_2 solely making up around 90% of those emissions. As a result of these emissions, the atmosphere generates a layer that absorbs heat from the sun, creating climate change as a result of global warming. Across the world, rising temperatures are endangering all life forms, including humans, by altering weather patterns and upsetting nature's delicate balance [15].
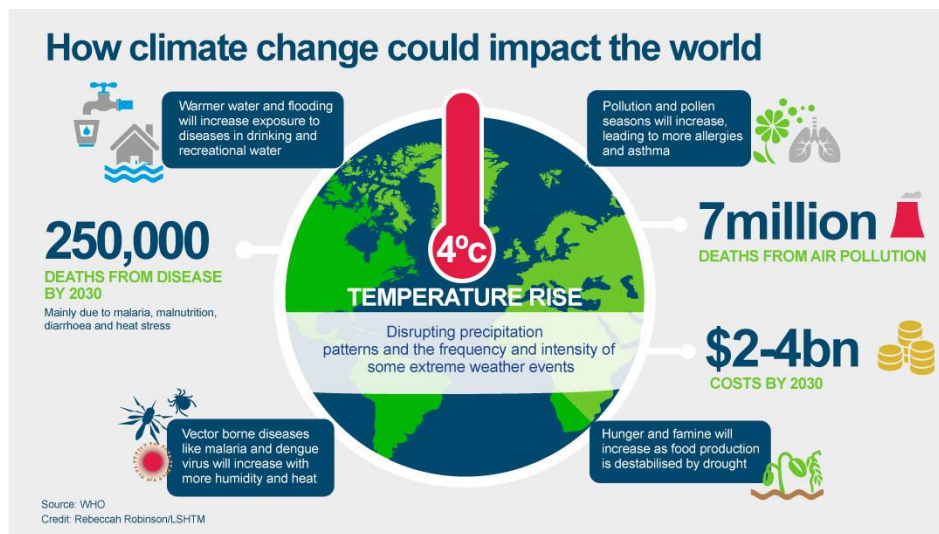
Figure 1.9: Impact of Climate Change in the World [14]

Assigning particular long-term causes to specific natural phenomena can pose a challenge, but certain consequences of recent climate change may already be observable. These include rising sea levels, shrinking glaciers, diminished Arctic ice, and disrupted agricultural patterns. forecast for secondary and regional repercussions encompass acute weather events, increased prevalence of tropical diseases, altered seasonal patterns in ecosystems, and significant economic implications. These concerns have spurred political activism, with calls for measures to mitigate, eliminate, or adapt to climate change.

1.7.2 Greenhouse Gas Emission Around the World

The release of GHGs, the primary driver of climate change, is an outcome of anthropogenic activities. China, the United States, and India collectively account for 42.6% of global emissions, which renders them the three biggest contributors. In contrast, only 2.9% of global emissions come from the bottom 100 nations. Agriculture

is the second-largest source of world emissions, accounting for close to 75% of them. The production of power and heat within the energy industry is the main source of emissions, followed by manufacturing and transportation. As they may both produce and absorb greenhouse gases and land use, are major sectors in the transition to a sustainable future and essential to reaching net-zero emissions [16].
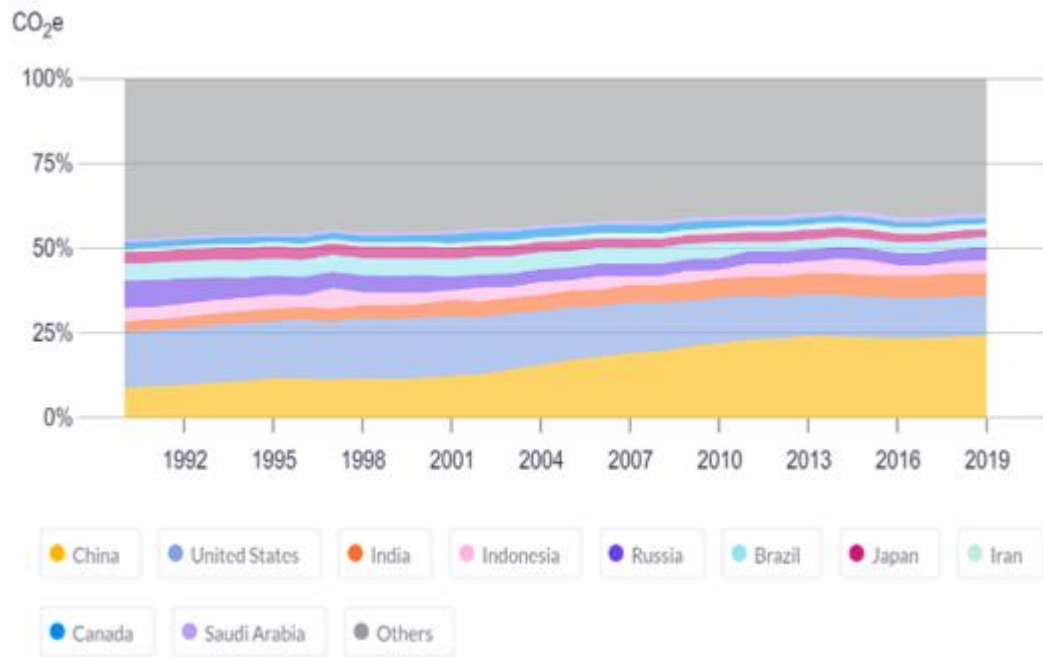
Figure 1.10: Green House Emission in the World [16]

1.7.3 Kyoto Protocol, Paris Agreement & COP 26

A notable international agreement to combat climate change was the Kyoto Protocol, which was enacted in 1997. It offered ground-breaking ideas like "carbon credits" and "carbon trading" and imposed binding emission reduction targets on developed nations. It presents three mechanisms to deal with its targets, specifically: emissions trading, the clean development mechanism, and joint implementation. Although the convention represented a big step forward, it mainly concentrated on developed countries and ignored large emitters from emerging nations.

In comparison, the 2015 Paris agreement is a more inclusive and comprehensive global climate pact. It establishes a long-term plan to keep the increase in global temperature well below 2°C and supports efforts to keep it below 1.5°C. The Paris Agreement, in contrast to the Kyoto Protocol, calls for contributions from all nations, not only developed ones, to cut emissions in accordance with their own plans known as

nationally determined contributions (NDCs). The agreement also places a focus on adaption strategies and offers assistance to underdeveloped nations.

The Conference of the Parties (COP) oversees both the Kyoto Protocol and the Paris Agreement. Significant discussions on a number of important topics, including phasing out coal, accelerating the use of renewable energy, and solving climate finance shortages, took place at COP 26. Hence, to accomplish the goals outlined in the Paris Agreement, the conference sought to reach a consensus on important priorities and policies. COP 26 emphasized the urgent need for more international cooperation and bold measures to reduce the devastating effects of climate change[17].

1.8 ROLE OF RENEWABLE ENERGY IN THE INDIAN ECONOMY

India has made impressive strides in its switch to renewable energy, with installed capacity rising dramatically from a few megawatts in 2010 to over 178.79 GW as of February 2023. This rise has been largely fueled by the nation's renewable energy goals and enabling policy environment. With the cancellation and retirement of multiple coal projects totaling more than 606 GW and 15.6 GW, respectively, from 2010 to 2022, India has also been actively lowering its reliance on coal-fired electricity. However, India's current account deficit has been negatively impacted by the country's growing reliance on imported coal as a result of domestic supply limitations and skyrocketing prices. The rise in coal costs has also contributed to inflation, which reached 15% in May/June 2022 according to the Wholesale Price Index (WPI). These difficulties emphasize how critical it is to reduce coal dependency and support India's ongoing energy transition [18].

The Institute for Energy Economics and Financial Analysis (IEEFA) and CEF (the India team of the Climate Policy Initiative) predict that renewable energy capacity would increase rapidly within India, with annual additions of 35–40 GW anticipated through FY2029–30, reaching a total of 405 GW. This increase is fuelled by factors such as competition from intermittent renewable energy sources, skyrocketing fossil fuel prices due to hyperinflation, and growing global commitments to capital investments through the Glasgow Finance Alliance for Net Zero (GFANZ). As a result, it is anticipated that thermal power generation will steadily lose market share, going from 72.3% in FY2021/22 to 53.4% in FY2029/30. These forecasts are bolstered by the aggressive capacity addition goals established by the government of India and promise

from numerous companies in sectors including power, oil & gas, steel, and cement. NTPC, a state-owned company, Adani Green Energy, Tata Power, ReNew Power, and Acme Solar are important players with total expansion capacity targets in the utility-scale category of roughly 231 GW by 2030. Therefore, to achieve its goals, the government of India is committed to promoting growth in the renewable energy sector. [18]. Figure 1.11 shows various factors that are key drivers for renewable energy capacity addition in India. In decentralized renewable energy, policy reforms and demand-side drivers are expected to drive significant growth in various segments.

Driver	Description
Commitment by Power Generating Companies	• ~220GW or 93% of India's incremental addition target of 236GW
Rooftop Solar	• Installed capacity of 11GW. Significant tailwinds from C&I decarbonisation pledges
Solar Pumps	• KUSUM target of 30.8GW. Opportunity set of 20 million grid connected agricultural pumps in India
Open Access Capacities	• Renewable energy open access market growing faster than the discom market
Hybrid Plus Storage Projects	• BESS costs projected to decline to US$58/kWh by 2030 strengthening the case for renewable energy plus storage
Merchant Capacities	• GoI aims to expand power markets to represent 25% share by 2025. Policy side reforms and market tailwinds
Offshore Wind	• Virtually non-existent in India but potential to install ~195GW of offshore wind capacity
Non-Power PSU Demand	• Combined target of 16.5GW by 2030 to decarbonise operations, and diversify business portfolio
Green Hydrogen Foray	• 5 MTPA production target by 2030 requires additional renewable energy capacity of ~118GW
Electric Vehicles	• US$ 375bn opportunity over the next 5 years in India providing a massive demand side trigger

Supply Side Drivers   **Demand Side Drivers**

Figure 1.11: Demand and Supply Side Drivers of Renewable Energy Capacity Addition in India [18]

The financial assistance of the Indian government, domestic corporations, and international investors strengthens the sector participants' capacity expansion goals. The forecast for renewable energy in India is generally favorable, with reduced regulations, dynamic market conditions, and high demand generating profitable returns and enabling the sector's explosive expansion.

Green hydrogen holds significant potential to propel India's clean energy aspirations on a large scale. With an aspiration of achieving 5 million tonnes per annum (MTPA) of green hydrogen production by 2030, India will need approximately 118 GW of additional renewable energy capacity. Corporate giants like Reliance Industries and

Adani Group have strongly embraced the green hydrogen policy, notified in June 2022, and have made substantial commitments towards achieving the 5 MTPA target [18].

1.9 NECESSITY OF FUEL CELLS

The above discussions highlight the pressing issues faced by India, namely the rapid drainage of fossil fuels and the environmental crisis. It is crucial to address these challenges promptly by decreasing reliance on petroleum-based fuels, which would have positive ramifications on both the environment and the economy. The usage of hydrogen in fuel cells as a clean and emission-free fuel for the twenty-first century has been extensively acknowledged by virtue of its outstanding prospects for energy efficiency and lack of emissions [19].

Fuel cells (FCs) have a variety of benefits over conventional combustion-based technologies, which are extensively used in autos and power plants. Compared to combustion engines, they operate more efficiently, instantly transforming the chemical energy of the fuel into electrical energy with a theoretical efficiency of more than 60%. In comparison to IC engines, FCs emit very little or none at all. Especially when used with hydrogen FCs, which produce only water, this substantially eliminates carbon dioxide emissions, one of the major climate issues. Additionally, at the site of operation, they do not produce air pollutants that lead to smog formation and health problems. FCs also have few moving parts, which makes them function silently [20]. There have been substantial improvements achieved in the use and functioning of fuel cells (FCs) since their inception in the 19th century. However, certain obstacles continue to stand in the way of their growth and usage in applications with high energy demands.

1.9.1 Historical background

The idea of FCs in 1839 while creating the first voltaic battery made of platinum and zinc foil plates was originated by Sir William Robert Grove [21], [22]. In this notion, two metals and two electrolytes were combined, with the producing metal having a higher attraction to the anion of the in-contact electrolyte as depicted in Figure 1.12 [23]. In 1889, Ludwig Mond and Carl Langer expanded upon Grove's notion by developing the fuel cell, a gas-powered battery. An electrolyte has been used between electrodes to build a gas-powered battery that could generate 2-2.5 A and 0.73 V [24]. Francis Bacon researched FCs in the 1930s with the goal of creating an affordable technology that could be used widely. Bacon used nickel electrodes to improve the

solubility of gases in alkaline systems [25] By 1959, FCs were being used to power a variety of devices, including forklift trucks, circular saws, and welding equipment [26]. The first proton exchange membrane fuel cell (PEMFC) was notably used during the NASA Gemini space mission, which took place between 1962 and 1966 and is often regarded as such. [27].
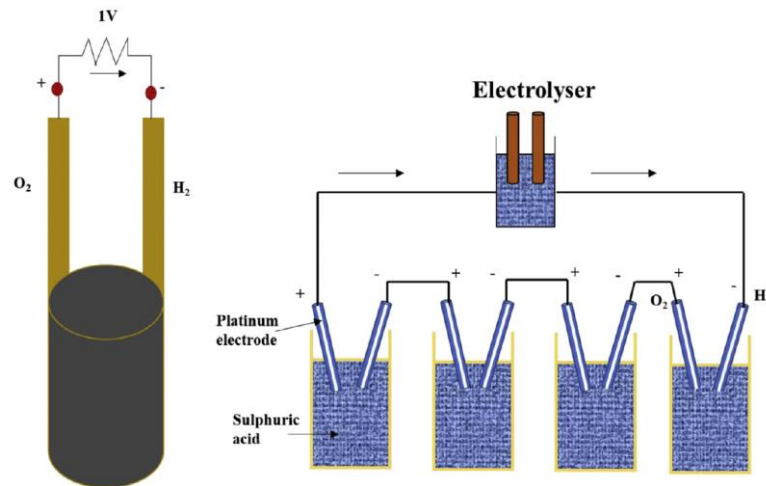
Figure 1.12: Gas Battery (left) and Gas Chain (right) Originated by Sir William Robert Grove's
[**23**]

1.9.2 FCs Concept

Figure 1.13 illustrates the functional concept of fuel cells (FCs), wherein each cell comprises two electrodes (anode and cathode) and a membrane-electrode-assembly (MEA) [28], [29]. The anode and cathode are made up of porous composite materials known as cermet, which is a combination of ceramics and metals, they facilitate the movement of gases between the channels and the electrolyte, while the MEA acts as a catalyst for the electrochemical reactions and facilitates the transfer of current flow. [30]. The anode of a fuel cell is where the fuel undergoes oxidation, while the cathode is where the oxidant undergoes reduction. The electrolyte within the fuel cell serves as a conductor for ions (such as H+ and O2-) at the same time allowing the flow of electrons. These electrons evolved through the anode reaction, and pass through an external circuit to reach the cathode, where they participate in the cathode reaction [31], [32].
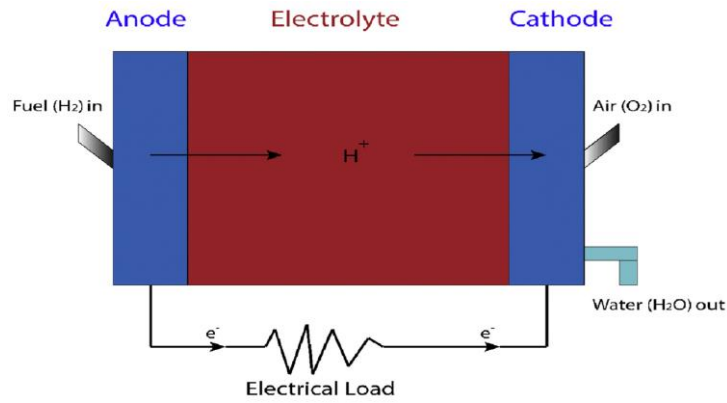
Figure 1.13: Basic principle of the FC.

There are various types of FCs, which are, PEMFC [33], phosphoric acid fuel cells [34] direct methanol fuel cells [35], molten carbonate fuel cells [36] alkaline fuel cells [37], microfluidic fuel cells [38] solid oxide fuel cells [39]. Comparative data on various FCs are included in Table 1.3:

Table 1.3. Comparison of Various Types of FCs [33]–[39]

S.No.	Types of FC	Fuel	Membrane	Oxidizer	Operational Temperature (°C)	Electrical Efficiency (%)
1.	Solid Oxide FC	H_2, CO	Ion conducting ceramic	O_2	1000	60
2.	Carbonate FC		Molten Alkaline melt	O_2; CO_2	650	50
3.	Phosphoric Acid FC	H_2	Phosphoric acid	O_2	200	40
4.	Direct Methanol FC	CH_3OH	Ion conducting polymer		80-110	50
5.	Proton Exchange Membrane FC	H_2			65-85	40-60
6.	Alkaline FC		Caustic potash		20-90	60

1.9.3 Applications of FCs

Fuel cells find diverse applications in the modern world, as outlined below [40]:-

➢ Power backup: They act as a power backup source when the main power supply is disrupted. Backup systems for manufacturing plants, household use, and computer networks are a few examples.

➢ More than 200 units of fuel cells from Ballard Industries are bought by Aditya Birla Group in September 2015 to power its telecom towers.

➢ Intelligent Energy obtained a €1.2 billion contract in September 2015 to provide fuel cells for 27,400 towers in India.

➢ A fuel cell-powered, zero-emission train called Coradia iLint was demonstrated by Alstom, a French rail vehicle manufacturer, in association with Germany and Canada.

➢ The first fuel cell-powered bus in India was to be introduced, according to a March 2018 announcement from TATA.

➢ Toyota Mirai, Honda FCX Clarity, Mercedes Benz F-Cell, and Hyundai ix35 FCEV are just a few of the fuel cell cars that have been created.

➢ By 2020, Toyota and Fuel Cell Energy hope to have a megawatt-scale carbonate fuel cell power plant up and running. It is situated near the port of Long Beach, California, and plans to produce 1.2 tonnes of hydrogen every day and 2.36 megawatts of energy each day.

➢ The Japanese government intends to build 35 hydrogen petrol stations in the city and put 6,000 fuel cell-powered vehicles on the roads in time for the 2020 Olympics in Tokyo. Tokyo will also see a rise in the number of buses powered by fuel cells.

➢ Aircraft with zero carbon emissions, such as the Lockheed CL-400 Sultan and HY4, also use fuel cell technology.

1.10 PROTON EXCHANGE MEMBRANE FUEL CELL

Proton exchange membrane fuel cells (PEMFCs) were created by "Niedrach and Grubb" in 1960 at "General Electric Company". Due to their small size and capacity to work at low temperatures, these fuel cells are extensively used. The Nafion polymer membrane used in the PEM fuel cell serves as a mediator in the electrochemical

process. Faster start-up and response times are made possible by the polymer membrane's solid-state properties, which lower reaction temperatures and increase efficiency. Placing a polymer separation membrane between two platinum electrodes with perforations eliminates the possibility of pollution. The PEMFC interacts at a temperature of around 80 °C, and the membrane conducts ions when it comes into contact with water [41], [42]. These cells have a high-power density relative to other cell types, with values ranging from 350-600 mW/cm^2, and their efficiency can reach 45–60%. Equations (1.1–1.3) describe the reactions in PEMFC.

At anode CL [43]:

$$H_2 \rightarrow 2H^+ + 2e^- \tag{1.1}$$

At cathode CL [43]:

$$2H^+ + 2e^- + \frac{1}{2}O_2 \rightarrow H_2O + \text{Heat} \tag{1.2}$$
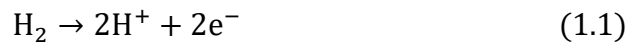
Overall Reaction [43]:
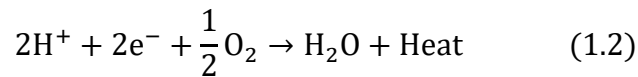
$$H_2 + \frac{1}{2}O_2 \rightarrow H_2O + \text{Electricity} + \text{Heat} \tag{1.3}$$

PEMFCs offer several benefits and drawbacks as listed in Table 1.4 below:

Table 1.4. Benefits and Drawbacks of PEMFC [41]–[43]

S.No.	Benefits	Drawbacks
1.	High energy density	Need of pure H2
2.	Compact design	Need of pure O2
3.	High specific power per unit weight and volume	Water flooding
4.	Quick start-up time	Costly
5.	Lower operating temperature	Platinum catalyst poisoning
6.	Easy and safe handling	
7.	Less maintenance (no moving parts) required	
8.	Uninterrupted electrical energy supply	

1.11 PRESENT WORK

The Fuel cell has been discussed in detail within the framework of the current study. Among them PEMFCs are widely researched and advanced fuel cell technology amongst all. Primarily due to the highly innovative and promising approach to power generation that offers significant benefits in terms of efficiency, environmental sustainability, and reliability. PEMFCs are an excellent solution for a number of uses, such as transportation, stationary power generation, portable electronics, and the space industry because of their quick start-up time, low operating temperature, and high-power density. PEMFCs are complex electrochemical systems that involve several different disciplines, including electrochemistry, materials science, fluid dynamics, and heat transfer. In the present era, outstanding progress has been made in developing high-performance PEMFCs. The performance of a PEMFC can be regulated by a variety of factors, counting the design and structure of the catalyst layer (CL), the gas diffusion layer (GDL), and the flow field Design (FFD). The FFD in a PEMFC is crucial to achieving optimal performance and large-scale commercialization. The FFD plays a vital role in ensuring that the reactant species i.e., oxygen, and hydrogen, are efficiently delivered to the electrochemical reaction sites, while also removing the product water that is generated during the reaction. A well-designed FFD can aid in better water and mass removal, homogeneous distribution of the physical quantities, reduced pressure drop, and low cost. A number of studies have been conducted to optimize and envisaged the FFDs, considering factors such as the geometry of the channels, the shape and size of the FFD, and the material considerations of the flow field. Overall, the design of flow fields for PEMFC is an evolving area of research, with the goal of developing cost-effective and efficient fuel cell systems for a range of applications. Hence, in the present work, an effort is made to develop the novel tapered-trapezoidal FFD for the straight parallel flow field.

CHAPTER 2

LITERATURE REVIEW

2.1 INTRODUCTION

As demarcated in the preceding chapter, the quest for renewable energy sources has gained momentum due to the escalating prices and uncertainties surrounding petroleum availability along with their effect on the environment. Researchers and scientists have been actively engaged in exploring viable alternatives, and one promising contender is the PEMFC. The PEMFC presents numerous advantages, including its renewable nature, eco-friendliness, and ease of production, particularly in rural areas where there is a pressing need for modern energy solutions. With its renewable nature, environmental friendliness, and potential to address energy security concerns, PEMFCs represent a significant step toward achieving a greener and more sustainable future. The continuous efforts of researchers and scientists worldwide are propelling the field forward, driving the development of efficient, durable, and cost-effective PEMFCs. As these advancements continue, the realization of widespread implementation and adoption of PEMFCs in various sectors is well within reach, ushering in a new era of clean energy generation.

2.2 FLOW FIELD DESIGN OF BIPOLAR PLATE OF PEMFC

A PEMFC consists of an intricately assembled suite of bipolar plates (BPPs), gas diffusion layers (GDLs), catalyst layers (CLs), and a proton exchange membrane (PEM) working together in unison [44], [45]. Among these components, the bipolar plates are of particular importance as they form the flow channels that distribute reactant gases [46], [47]. The membrane electrode assembly (MEA) is analogous to the heart of a fuel cell, while the BPPs serve as a means to distribute gases (hydrogen and air) and facilitate the efficient transport of electricity, similar to veins [48]. It comprises 45% of the stack cost and 80% of the total weight of the stack [49]. The main functions and requirements of BPPs are summarized as follows [43], [50], [51]: -

- The BPP bolsters the MEA by giving the PEMFC as a whole adequate mechanical strength. It must therefore have enough strength. Additionally, selecting materials with higher specific strength will improve power density.
- The surface of the BPP requires processing to create a flow field, which acts as channels for gas and water. Hence, it is crucial to maintain good processing capabilities.
- Excellent electrical conductivity is required for the BPPs to function as a current collector and conductor.
- The BPP is expected to properly separate the oxidant and the reducing agent by exhibiting low gas permeability.
- Since the PEMFC's electrolyte is an acidic medium, the BPPs resistance to chemical and electrochemical corrosion must be excellent in order to prolong its life of it.
- The BPP should have a low thermal expansion coefficient and excellent thermal conductivity because the fuel cell's internal operating temperature is around 80 °C.
- The BPP needs to be inexpensive in order to be appropriate for mass commercial manufacture.

The FFD pertains to the shape and structure of the channels found in the BPP. It's absolutely essential to keep in mind that these channels can be made using machining operations (often used for graphite plates) or formed using a variety of approaches (such as die stamping, forming, and other methods, typically used for BPPs made of metal) [52]. The purpose of the flow field is to deliver the necessary amounts of reactants to the GDL and the CL while minimizing the drop in pressure on the cathode and anode sides, respectively. High electrical and thermal conductivity, robust material strength to endure clamping pressure, non-toxicity, water resistance, and ease of machining are among the crucial properties of flow field materials [53]. The flow field plates used for this function are frequently made of stainless steel or plain graphite, with graphite being the material of preference. In addition to providing reactants to the anode and cathode sides, these FFD also facilitate the movement of water and electrons from and to the CL. A well-designed flow field enhances water management and overall performance by preventing water flooding in the cathode [53].

Various flow field patterns are widely utilized in PEMFC, exhibiting notable differences. These include patterns characterized by single straight, parallel, serpentine, interdigitated, pin, cylindrical, spiral, radial, square, natural-inspired, tubular, and fractal designs. Figure 2.1 illustrates the flow field designs that are commonly employed in PEMFC. The performance of PEMFC is significantly influenced by the design of the flow field, prompting numerous modifications aimed at enhancing its effectiveness [53].
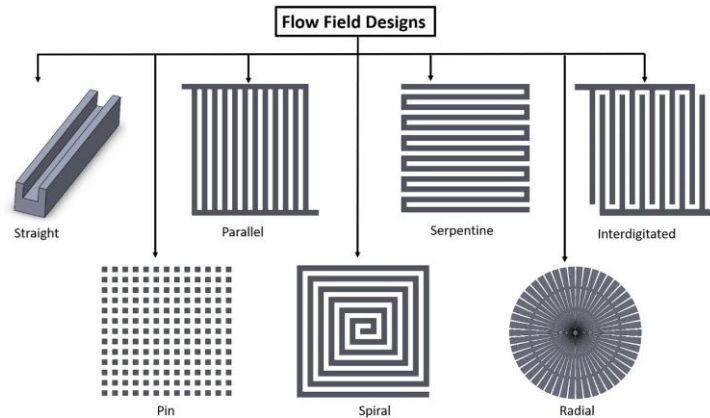
Figure 2.1: Different Types of Flow field Design

The use of parallel, serpentine, interdigitated, or a combination of these flow fields is a commonly employed practice in the production of FFDs for commercial PEMFCs [54], [55]. Parallel FFDs have a low-pressure drop due to reactant diffusion, but may not provide enough reactant supply or efficient water removal, leading to poor performance. While serpentine [56] and interdigitated [57] FFDs enhanced water extraction and reactant distribution rates at the expense of high pressure decreases and decreased energy efficiency due to pumping loss. To sum up, each of the three FFDs - parallel, serpentine, and interdigitated - has its own set of advantages and disadvantages when utilized in PEM fuel cells. A lot of effort has been invested in enhancing the efficiency of the aforementioned fundamental designs, with the aim of achieving better performance. Therefore, this literature review evaluates different FFDs for PEMFCs, such as conventional, modified, novel, and nature/bio-inspired designs, and their merits and demerits. The literature review also examines the state of the art of FFDs and provides important observations, giving valuable insights into recent trends in PEMF's FFD, which may help in the development of the new FFDs.

2.3 LITERATURE REVIEW

Cooper et al. [57] created bipolar plates with varying cross-sectional sizes and conducted experiments to confirm that the performance of the plates in PEMFC is greatly influenced by the proportion of channel width to rib width in both parallel and interdigitated channels. This ratio plays a pivotal role in determining their performance.

Hamrang et al. [58] thoroughly investigated the performance of two FFD types, namely the parallel serpentine flow field (PSFF) and the parallel serpentine-baffled flow field (PSBFF) with a blocked exit channel, which was evaluated to assess the influence of operational and geometric parameters. The findings indicated that the PSBFF design exhibited superior performance in comparison to the PSFF design.

Li et al. [59] developed a methodology to optimize the parallel FFD in a PEMFC by partially blocking a channel. The results of the study demonstrate that optimizing the channel led to an improvement of approximately 10.9% in the net power output of the PEMFC.

Gong et al.[60] focused on the multi-stage Tesla valve (MSTV) flow field in PEMFCs and aimed to evaluate the transport properties and performance of both forward and reverse flow. It has been discovered that at high-load situations, the MSTV-Reverse FFD's current density distribution is more homogenous, which can effectively counteract local fuel starvation.

Lin et al. [61] examined the key-shaped 3D FFD on both performance and mass transfer. The researchers compared a conventional straight single FFD with a new channel and found that the latter improved performance by up to 30%.

Yang et al.[62] studied two different geometrical parameters of the M-shaped flow channel in PEMFCs and found that the M-shaped flow channel gives enhanced mass transfer without the cost of the high drop in pressure.

Dang et al. [63] introduced three distinct designs for the cathode of a PEMFC, each of which utilized pin-type FFD with circular, square pins, and diamonds. The researchers concluded that square pins remove water faster but create more pressure than streamlined or rounded pins.

Monsaf et al. [64] developed a FORTRAN program was developed to examine the effects of channel width, the number of turns in the spiral channel, and flow direction on reactant dissipation in a PEMFC utilizing a spiral flow field design. The program was designed to investigate how these parameters impact the dissipation of reactants within the fuel cell.

Suarez et al. [65] in their study explored new FFDs that were inspired by lungs, leaves, and sponges, each of which had distinct characteristics. The newly proposed biomimetic design demonstrated superior performance when working at higher relative humidity levels of 90%, achieving a peak power output that was 6.0% higher. This suggests that the novel biomimetic FFD is especially effective at improving water management when dealing with high reactant humidity conditions.

Dang et al. [66] studied a symmetrical leaf-shaped FFD based on Murray's Law. The literature suggests that this design results in a superior drop in pressure than the traditional FFDs, which can enhance the performance of fuel cells.

Ascencio et al. [67] set up a numerical model in three dimensions and an entropy generation analysis was created for a PEMFC with tree-like FFDs. The objective of the study was to identify a geometry that facilitates a uniform scattering of species within PEMFC. The results show that the angles and number of bifurcations have remarkable effects on the various operational parameters of the PEMFC.

Alvarado et al. [68] examine the significance of flow distribution homogeneity and the impact of channel area by modeling the constructal design, as a gas distributor in both electrode sections of a PEMFC. The aim is to inspect the role of this design in the performance of the fuel cell. The findings presented in the study indicate that the suggested flow configurations based on constructal theory are unsuitable for serving as BPPs in fuel cell applications.

Oedegaard et al. [69] aim to explore the impact of fractal FFD on the transport properties of PEMFCs and, consequently, the stability of FCs operations. It was proposed that utilizing fractal structures could be a beneficial substitute.

Huang et al. [70] present five distinct flow channel structures with baffles in straight parallel flow fields and compare their mass transfer and performance in PEMFC using the CFD solution. The results indicate that the PEMFC equipped with a

cylindrical baffle that includes a cut performs the most effectively, achieving an output current density of 1.82 A/m^2 at a voltage of 0.4 V.

Zuo et al. [71] introduces a novel configuration was introduced for PEMFC, which involved staggered blocks placed on the parallel flow channels along with auxiliary flow channels beneath the ribs. The findings demonstrate that at an operating voltage of 0.5 V, the current density achieved by the proposed structure is 21.74% higher compared to the conventional SPFF design. Furthermore, the power density of the proposed structure is measured to be 0.65 Wcm^{-2}.

Zhang et al. [72] observed a new FFD that enhances the performance and improves the mass transfer of the FC. The new FFD exhibits an enhancement of approximately 25.2% in the total power density compared to the conventional design when operating at the same output current density of 2.0 A/cm^2. It also improves the cross-flow beneath the surface and increases the effective mass transfer coefficient.

Chen et al. [73] present a novel stepped FFD for PEMFC bipolar plates that aims to enhance several operational and electrical parameters of PEMFC. The study examines the distribution of water content, oxygen concentration, liquid water saturation, and gas velocity within FCs to assess the efficacy of this particular design. The results indicate enhancement in the distribution of liquid water and alleviating water flooding issues at the interfaces of GDL/CL and CL/MEM.

Pashaki et al. [74] evaluated the numerical analysis conducted to evaluate the performance of a curved (arc-shaped) PEMFC in comparison to a straight (planar) PEMFC. The study revealed that the curved design exhibited higher average current density and total current at the same operating voltage. Despite generating more water due to the increased electrical current, the bent PEMFC demonstrated slightly lower water content due to improved water removal through convection.

Wang et al. [75] developed a tapered parallel FFD to enhance the species transport, water drainage, and overall performance of FCs. The study examines the effect of the ratio between the side length of the inlet and that of the outlet ($L_{I/O}$) in the new FFD design by analyzing the distribution of internal physical quantities within the PEMFC. The result shows the PEMFC with ($L_{I/O}>1$) gives a superior performance as compared to ($L_{I/O}<1$).

Chen et al. [76] conducted an analysis of a PEMFC that was non-isothermal and multi-phase, three-dimensional, and used a single straight channel. Through optimization, a trapezoidal channel was determined to be the optimal channel. The power density of the FC in the optimal channel was found to increase by 4.43%.

2.4 OUTCOMES OF LITERATURE REVIEW

As an outcome of review of literatures, the following major findings can be drawn;

➢ As the conventional FFDs have become stagnant, hence further research into them will be futile. Researchers have found that the serpentine flow field is more efficient than parallel and interdigitated flow fields but due to a large pressure drop more pumping power is required.

➢ The design of modified FFDs is not constrained by size or structure and thus has a high potential for development. The modified FFDs formed through dimensional optimization of conventional FFDs have limited potential for improvement in fuel cell performance, service life, or costs due to constraints within conventional designs

➢ The FFDs with obstacles or baffles are a significant branch of the modified FFDs, and the addition of baffles to conventional FFDs can improve performance cost-effectively. However, there is limited research space left for optimizing conventional FFDs with baffles, and further development requires exploring different forms, layouts, and parameter optimization.

➢ The innovative FFDs have also shown unprecedented performance improvement in PEMFCs. Due to the emergence and rapid development of innovative FFD, conventional FFDs are still favored for their ease of manufacturing and low cost, hence innovative FFDs have significant potential for development and require further optimization

➢ the nature/bio-inspired FFDs have yet to demonstrate significant performance improvement, advanced materials, and manufacturing processes offer potential for bio-inspired designs such as fractal FFDs to achieve a leap in performance in the future. Therefore, further research on nature/bio-inspired FFDs should not be abandoned.

➢ Mass transport of reactants and products improved by converging or diverging the flow field Channel.

- ➢ Exhaustive studies suggest that every flow field design has its own merits and demerits.
- ➢ Researchers optimized a straight parallel FFD because of its easy fabrication.
- ➢ Tapering the conventional FFD improves the results of PEMFC.
- ➢ A trapezoidal straight parallel flow field gives more homogeneous current density and improved water removal from the cathode side.
- ➢ Very little quantum of investigation has been done for the trapezoidal cross-section with converging or diverging straight parallel flow field design.

2.5 RESEARCH GAP ANALYSIS

After the exhaustive review of the literature, the following research gaps were identified:

- ➢ Despite enormous studies on the FFDs, the effect of the trapezoidal cross-section with converging or diverging straight parallel flow fields has been less unexplored.
- ➢ The effect of these FFDs on the diffusion of reactants and products into the GDL is to be studied.
- ➢ It is necessary to examine the relationship between cell performance and the pressure drop along the flow channel.
- ➢ How well the water is drained from the fuel call needs to be studied.
- ➢ The effect of operating parameters like temperature and pressure should be optimized for better performance.

2.6 RESEARCH OBJECTIVES

The following objectives were envisaged for the present research work:

- ➢ Study of Existing Straight Parallel FFD of PEMFC and identification of current design Flaws and pathways for it's improvement.
- ➢ Development of the new trapezoidal cross-section with converging or diverging straight parallel flow field.
- ➢ Evaluation of V-I characteristics of new flow field design and its comparison with existing Parallel FFD.
- ➢ To study the effect of temperature distribution, reactants distribution, pressure drop, and water removal capability on the performance of new FFD.
- ➢ Optimization of geometric dimensions of new flow field design for higher current and power density.

CHAPTER 3

MODEL DEVELOPMENT AND COMPUTATIONAL PROCEDURE

3.1 INTRODUCTION

Fuel cells are sophisticated systems that simultaneously include, electrochemical, physical, and mechanical processes. Effective improvements in FC performance, efficiency, and manufacturing costs can be made with the help of a comprehensive knowledge of these complicated phenomena. For understanding the FC devices and the processes they are related to, pragmatic modeling and experimental verification techniques are effective mechanisms. Despite the fact that experimental approaches are typically regarded as superior and more reliable, cost and time restrictions have led to a preference for modeling. It is crucial to precisely measure the impact of current density because it has a large impact on FC performance [77], [78]. Nevertheless, there are several drawbacks to using experimental methods. For instance, it becomes difficult to quantify the impact of current density on fuel cell efficiency when there are only slight modifications. Additionally, even while experimental methods can generate data and create V-I polarisation curves, pinpointing the factors that affect the curve's shape is incredibly challenging, especially when fuel cells are working in a variety of environments. However, modeling methods have a number of advantages when it comes to simulating the impacts of various FC parameter values. However, the analytical models used for fuel cells are sometimes overly idealized and simplified. They frequently decrease the model's dimensions to zero or one, simplifying the underlying physics through the linearization of the equations, which would otherwise prevent them from being solved analytically. As a result, analytical models become less accurate, especially when dealing with large current densities. For estimating voltage-current relationships and performing rapid computations on simpler systems, analytical methods are preferable [79]. Under ideal circumstances, analytical models can offer the fundamental perspective.

3.2 THERMODYNAMICS OF PEMFC

The inquiry into the nature of the electrochemical, thermal, and electrical reactions occurring inside the fuel cell is covered by thermodynamic fuel cell analysis. Understanding these reactions' foundational mechanisms and how they interact enables researchers to evaluate the FCs' effectiveness and performance. The term "Gibbs-free energy" describes the energy that can be used to carry out external work, excluding any work involving adjustments to pressure or volume. Gibbs free energy per unit mole is written as [80],

$$\Delta g = \Delta h - T\Delta s \qquad (3.1)$$

Hydrogen and oxygen gases react in PEMFCs as discussed in Equation (1.1-1.3), and this reaction produces water so the Gibbs free energy of formation for the electrochemical reaction becomes:

$$\Delta g_f = \Delta g_f(\text{Product; H2O}) - \Delta g_f(\text{Reactant; H2}) - \Delta g_f\left(\text{Reactant; } \frac{1}{2}\text{O2}\right) \qquad (3.2)$$

The Gibbs Free energy does not entirely transform into electrical energy when it enters the cell, even if losses are neglected. As for each H_2 molecule, two electrons pass around the external circuit. Hence, the charge that passes through the external circuit for one mole of H_2 can be expressed as;

$$2e * N = 2F \qquad (3.3)$$

In the equation, "e" represents the charge carried by electrons, and "N" denotes Avogadro's number ($6.023*10^{23}$), and "F" represents Faraday's constant, which is equivalent to 96,487 J/V-mole. If E is the voltage of the FC, then the electrical work originated with the charge flowing in the circuit is

$$W\left(\frac{J}{mol}\right) = -2F\left(\frac{C}{mol}\right) * E\left(\frac{J}{C}\right) \qquad (3.4)$$

The electrical work achieved in a reversible system is equivalent to the Gibbs free energy released according to equation (1.3) [81], [82] ;

$$\Delta g_f^-\left(\frac{J}{mol}\right) = W\left(\frac{J}{mol}\right) = -2FE\left(\frac{J}{mol}\right) \qquad (3.5)$$

This leads to the reversible open circuit voltage (OCV), or electromotive force (EMF).

$$E_o = E = \frac{-\Delta \bar{g_f}}{2F} \qquad (3.6)$$

The OCV corresponds to the actual operating conditions during fuel cell operation at a specific temperature. It is influenced by the changes in Gibbs energy that occurs when the reactants enter the cell and interact with the operating parameters. These factors are depending on the electrochemical reactions which take place within the FCs. The Nernst equation establishes the correlation between the OCV (E_o) under standard conditions and the operating voltage (E) of FC at varying temperatures and pressures.

$$E = E_o + \frac{RT}{2F} \ln \left(\frac{P_{H_2} \cdot P_{O_2}^{\frac{1}{2}}}{P_{H_2O}} \right) \qquad (3.7)$$

In the equation, "R" represents the gas constant (8.314 KJ/K-mol), "T" denotes the temperature in Kelvin, and "P" signifies the gas pressure in both the anode and cathode (in bar). Therefore, the Nernst equation gives the dependency of OCV in the pressure of reactants and products of the PEMFC as well as on the operating temperature of the PEMFC [80].

3.3 POLARISATION PHENOMENON

Under load conditions, the voltage of the FC decreases by around 60% to 70% compared to the OCV. The V-I curve characteristics are determined by both the output voltage and current density. The output voltage of a PEMFC is closely linked to the thermodynamically speculated voltage in FCs, taking into account three main types of losses: activation losses, ohmic losses, and concentration losses. Activation losses arise from the electrochemical reactions taking place, ohmic losses stem from ionic and electronic conditions, and concentration losses occur due to species mass transport [83]. It is clear from Figure 3.1 that the OCV (Eo) is lower than the reversible voltage's predicted value [83]. Fuel crossover and internal currents across the electrolyte, which should ideally only permit ion movement, are the main causes of this loss. The PEM does, however, conduct only a modest amount of fuel and electrons. The polarisation curve shows how this conductivity of fuel and electrons through the electrolyte reduces

the OCV. Due to activation losses brought on by the sluggishness of the reaction going on the electrode surfaces, the voltage decreases initially and quickly as the current deviates from zero. As it drives the chemical reaction that drives electrons to and from the electrode, some of the voltage generated is lost. The voltage losses show a linear pattern and decrease more slowly at moderate current densities. These linear features represent ohmic losses, also known as "resistive losses," which result from the resistance that ions in the electrolyte and electrons encounter when moving through various fuel cell components.
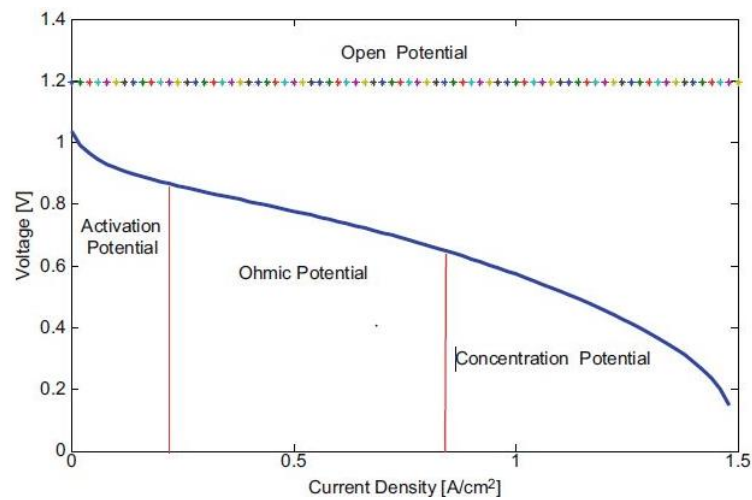

Figure 3.1: The Schematic Diagram of Polarization Curve and Three Losses

The linear pattern of the voltage drops and its relationship to the current density are both present. However, due to restrictions on mass movement within the fuel cell, the voltage rapidly decreases with greater current densities. These restrictions, also known as "mass transport or concentration losses," are brought on by changes in the concentration of reactants at the electrode surfaces. These variations in concentration can be caused by a number of variables [80]:-

1. A barrier that prevents the gases from getting to the membrane's active areas.
2. The augmentation of water products obstructing the flow channels within the BPPs or the GDL. To prevent a significant decrement in power density in this region, it is recommended to operate the FC system at its peak power density.

The following parts contain a thorough treatment of the modeling of geometry, creation of numerical models, discretization method, boundary conditions, and model validations.

3.4 MODEL ASSUMPTIONS

The model created for this research is a three-dimensional, steady-state, single-phase model for a PEMFC. This work makes use of the following model assumptions in order to streamline and effectively solve the model [75], [84], [85]:-

- The model assumes that all gases follow the ideal gas equation.

- The flow has a low Reynold number in the PEMFC i.e., laminar flow.

- Water is considered to be in the gaseous phase.

- A thoroughly humidified membrane is expected.

- The materials of membrane, electrode, and GDL are isotropic.

- The resistance to thermal and electrical contact is not taken into account.

3.5 GEOMETRY MODELS

Figures 3.1 illustrate diagrams of the PEMFC featuring conventional, tapered, and novel tapered-trapezoidal straight parallel FFDs. In the case of the conventional straight parallel FFD, the dimensions of the ribs and channels are 1.0 mm in height and width, respectively, and 50.0 mm in length is the same as that in the reference [75]. Table 3.1 presents the PEMFC geometrical properties.

Table 3.1 Geometrical Features of PEMFC [75]

Geometrical Parameters	Numerical Value
Channel length, width, height	50mm, 1mm, 1mm
Land width length, width, height	50mm, 1mm, 1mm
Thickness of GDL	0.2mm
Thickness of CL	0.02mm
Thickness of MEM	0.005
Reactive area	1 mm^2

For the present study, an optimum tapered flow field ($L_{I/O}$=1.6) is taken from the reference [75] shown in Figure 3.2 (2.) as case C2. The electrode (both anode and cathode) BPs are adjusted for the novel tapered-trapezoidal straight parallel FFDs. In this study, three distinct types of tapered-trapezoidal FFDs are created by varying the dimensions of the parallel sides, namely "a" and "b" at the inlet, as illustrated in Fig.3.2 (6.). It should be mentioned that the novel tapered-trapezoidal straight parallel FFDs possess the same inlet cross-sectional area, inlet height, and length of PEMFC comparable to those of the conventional straight parallel FFD. As a result, this

simulation study will examine three variations of tapered-trapezoidal FFDs, which are differentiated by the dimensions "a" and "b" of the proposed FFD, in order to keep the same inlet cross-sectional area and inlet height, which are shown in Table 3.2. Figure 3.3 presents a diagrammatic representation of a geometric model, illustrating the inlet and outlet at both electrodes. On the other hand, Figure 3.4 illustrates the schematic diagrams of a PEMFC, emphasizing the computational domains and the specifically generated mesh for case C1. Additionally, Figure 3.5 presents the schematic diagrams of a PEMFC, demonstrating the computational domain and mesh generated for the remaining cases, namely C2, C3, C4, and C5.
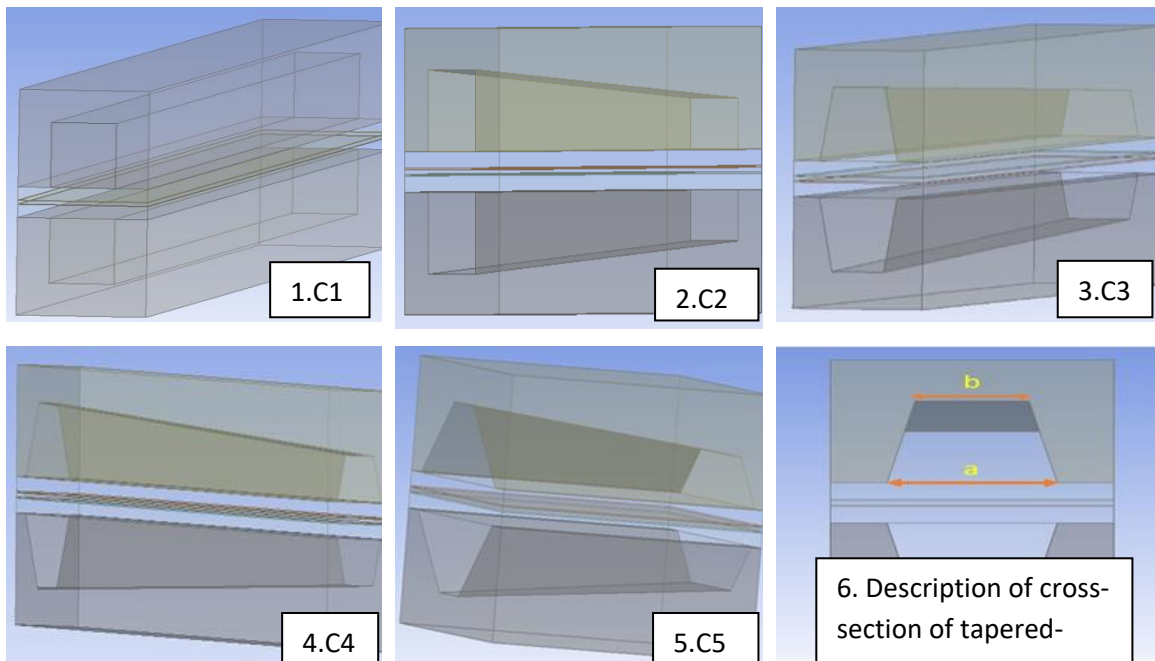

Figure 3.2: Geometrical Model of Different Cases 1.C1, 2.C2, 3.C3, 4.C4 & 5.C5 and 6. Description of cross-section of Tapered-Trapezoidal FFDs

Table 3.2 Specifications of the Modelled Cases for the Different Designs

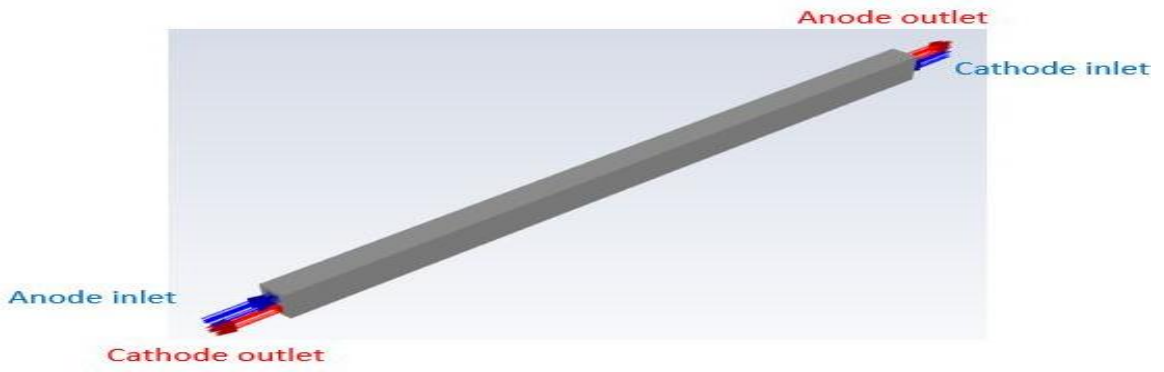| Case	Types of FFD	Description
C1	Conventional Straight Parallel FFD	-
C2	Tapered Straight Parallel FFD	a = 1.00mm; b = 1.00mm
C3	Tapered-Trapezoidal Straight Parallel FFD	a = 1.20mm; b = 0.80mm
C4	Tapered-Trapezoidal Straight Parallel FFD	a = 1.40mm; b = 0.60mm
C5	Tapered-Trapezoidal Straight Parallel FFD	a = 1.60mm; b = 0.40mm

Figure 3.3: Schematic of Geometrical Model showing the Inlet and Outlet at Anode and Cathode side
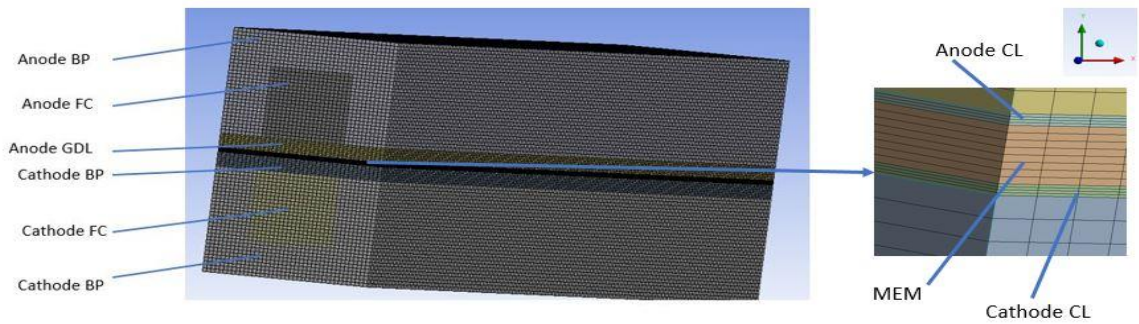

Figure 3.4: Schematics of a PEMFC with Computational Domain and Mesh Generated for the C1
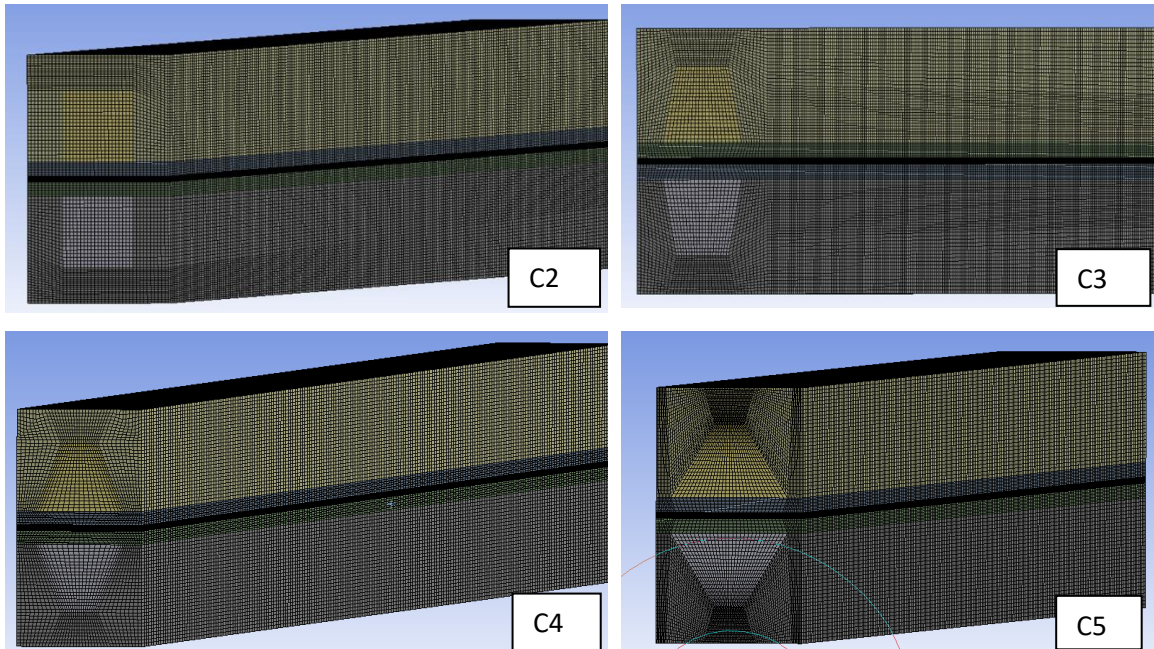

Figure 3.5: Schematics of a PEMFC with Computational Domain and Mesh Generated for the C2, C3, C4, & C5

3.6 NUMERICAL MODELS

The PEMFC is a complex system that involves multiple physical processes occurring simultaneously during its operation. These processes include the transfer of substances such as hydrogen, oxygen, and water, which is linked to the flow of fluid, as well as the transfer of heat and the occurrence of electrochemical reactions.

A mathematical model of a PEMFC is created that accurately represents its behavior, and a three-dimensional CFD model is employed. This model takes into account various equations, including those related to mass conservation (Eq. 3.8 to 3.12), Navier-Stokes equations (Eq. 3.13 to 3.14), species transport (Eq. 3.15 to 3.16), energy (eq. 3.17 to 3.18), and electrical charge (eq. 3.19 to 3.23). Additionally, Butler-Volmer equations are incorporated into the model to describe the electrochemical reactions (eq. 3.24 to 3.28) occurring in the catalyst layers.

Mass conservation equations [86]–[88]

$$\vec{\nabla} \cdot (\rho \vec{u}) = S_{H_2} + S_{O_2} + S_{H_2O} \tag{3.8}$$

In the equation, the density of the gas mixture, denoted as ρ, is calculated by using the ideal gas equation as indicated in equation (3.9) [87].

$$\rho = \frac{P}{RT\sum \frac{Y_i}{M_i}} \tag{3.9}$$

The equations (3.10) to (3.12) are used to compute the source terms for the utilization of hydrogen and oxygen, as well as the production of water [86], [88], [89].

$$S_{H_2} = -\frac{j_{an}}{2F} M_{H_2} \tag{3.10}$$

$$S_{O_2} = -\frac{j_{ca}}{4F} M_{O_2} \tag{3.11}$$

$$S_{H_2O} = +\frac{j_{ca}}{2F} M_{H_2O} \tag{3.12}$$

Momentum conservation equations[90], [91];

$$\vec{\nabla} \cdot (\rho \vec{u} \vec{u}) = -\vec{\nabla}P + \vec{\nabla} \cdot (\vec{\nabla}\mu \vec{u}) + S_u \tag{3.13}$$

The momentum equation's source term is determined by Darcy's law in porous media and can be represented by equation (3.14) [62];

$$S_u = -\frac{\mu}{k_p} \varepsilon \vec{u} \tag{3.14}$$

Species conservation equations [92]

$$\vec{\nabla} \cdot (\rho \vec{u} Y_i) = \vec{\nabla} \cdot \left(\rho D_i^{eff} \vec{\nabla} Y_i\right) + S_i \tag{3.15}$$

The equation for the source term, S_i, was described in equations (3.10) to (3.12). The effective reactant species diffusivity (D_{eff_i}) is obtained from eq. (3.16) [93], [94];

$$D_i^{eff} = \varepsilon^{1.5} D_i \tag{3.16}$$

Energy conservation equations [87]

$$\nabla \cdot \left(\rho C_p \vec{u} T\right) = \nabla \cdot (k_{eff} \nabla T) + S_h \tag{3.17}$$

Where, S_h is the source term of the energy equation [71]. It contains $I^2 R_{0hm}$, h_{react} and $j_{an.ca} \eta_{an.ca}$ which refers to the following factors contributing to the overall heating: ohmic heating, the heat generated from electrochemical reactions, and the product of the overpotential and transfer current in the cathode or anode catalyst layers, respectively.

$$S_h = I^2 R_{0hm} + h_{react} + j_{an.ca} \eta_{an.ca} \tag{3.18}$$

Electric charge conservation equation [86], [93], [94];

$$\nabla \cdot (\sigma_{sol} \nabla \varphi_{sol}) + S_{sol} = 0 \tag{3.19}$$

$$\nabla \cdot (\sigma_{mem} \nabla \varphi_{mem}) + S_{mem} = 0 \tag{3.20}$$

The equation (3.21) provides an empirical correlation for obtaining the membrane conductivity, which is referred to as S_{mem} [95]

$$\sigma_{mem} = [0.514\lambda - 0.326] \exp\left[1268\left(\frac{1}{303} - \frac{1}{T}\right)\right] \tag{3.21}$$

Equations (3.22) and (3.23) describe the connections between the source terms of the phase potential equations and the transfer current densities [87], [96];

$$S_{sol} = -j_{an.ca} \tag{3.22}$$

$$S_{mem} = j_{an.ca} \tag{3.23}$$

Electrochemical reactions [87], [88] in the Butler-Volmer model, the volumetric transfer current densities at the electrode (both anode and cathode) sides are given by equations (3.24) and (3.25), respectively.

$$j_{an} = \xi_{an} j_{an}^{ref} \left(\frac{C_{H_2}}{C_{H_2}^{ref}} \right)^{\gamma_{an}} \left(\exp\left(\frac{\alpha_{an}F}{RT} \eta_{an} \right) - \exp\left(\frac{-\alpha_{ca}F}{RT} \eta_{an} \right) \right) \tag{3.24}$$

$$j_{ca} = \xi_{ca} r_{ca}^{ref} \left(\frac{C_{O_2}}{C_{O_2}^{ref}} \right)^{\gamma_{ca}} \left(-\exp\left(\frac{\alpha_{ca}F}{RT} \eta_{ca} \right) + \exp\left(\frac{-\alpha_{ca}F}{RT} \eta_{ca} \right) \right) \tag{3.25}$$

The driving force behind the electrochemical reaction is the surface over-potential, which represents the disparity between the phase potentials of the solid (which facilitates electron conduction) and the electrolyte (which facilitates proton conduction). The activation over-potentials at the electrode (both anode and cathode) sides, represented by η_{an} and η_{ca} respectively, are calculated using equations (22) and (23) [87], [93], [94].

$$\eta_{an} = \varphi_{sol} - \varphi_{mem} \tag{3.26}$$

$$\eta_{ca} = \varphi_{sol} - \varphi_{mem} - V_{OC} \tag{3.27}$$

Equation (3.28) shows an approximation for the OCV of the overall reaction [94].

$$V_{OC} = E_0 + \frac{RT}{2F} \ln \left[\frac{P_{H_2} P_{O_2}^{0.5}}{P_{H_2O}} \right] \tag{3.28}$$

Equation (3.29) governs the process of water transport through the PEM, which is caused by electro-osmotic drag, water concentration gradient, and pressure gradient force [53], [94], [97].

$$\vec{\nabla} \cdot \left(\frac{n_d \cdot M_{H_2O}}{F} \vec{I} - D_W \vec{\nabla} C_W - C_W \frac{k_p}{\mu_{H_2O}} \vec{\nabla} P \right) = 0 \tag{3.29}$$

Equations (3.30) to (3.32) are used to calculate the electro-osmotic drag coefficient, water diffusivity, and water mass concentration, respectively[53], [94], [97].

Equation (3.33) is used to decide the water content of the membrane, while Equation (3.34) is used to find out the water activity[94].

$$n_d = 2.5 \frac{\lambda}{22} \tag{3.30}$$

$$D_W = \begin{cases} 3.1 \times 10^{-7}\lambda[\exp(0.28\lambda) - 1]\exp\left[-\frac{2346}{T}\right] & \lambda \leq 3 \\ 4.17 \times 10^{-8}\lambda[1 + 161\exp(-\lambda)]\exp\left[-\frac{2346}{T}\right] & \lambda > 3 \end{cases} \tag{3.31}$$

$$C_W = \frac{\rho_{m.dry}}{M_{m.dry}}\lambda \tag{3.32}$$

$$\lambda = \begin{cases} 0.043 + 17.81a_w - 39.85a_w{}^2 + 36a_w{}^3 & 0 < a_W < 1 \\ 14 + 1.4(a_w - 1) & 1 \leq a_w \leq 3 \end{cases} \tag{3.33}$$

$$a_w = \frac{X_{H_2O}P}{P_{sat}} \tag{3.34}$$

3.6.1 Boundary Conditions

The boundary conditions and calculation region for the 3D model must be established before carrying out the numerical simulation. The operational pressure for the gas outlets, which are denoted as pressure outlets, is set at 1 atm. The cathode and anode gas inlets, on the other hand, are calculated using equations (3.35) and (3.36) and are defined as mass flow inlets [75]. A uniform temperature of 343.15 K was assigned to the external walls, as well as the anode and cathode inlets, to maintain a constant temperature. The determination of the molar concentration of reactant gas species involves considering factors such as temperature, relative humidity, and operating pressure. Table 3.3 outlines the primary parameters discussed in this paper.

$$m_a = \frac{\rho_g^a I_{ref}\zeta_a A}{2F_{C_2}} \tag{3.35}$$

$$m_c = \frac{\rho_g^c I_{ref}\zeta_c A}{4F_{O_2}} \tag{3.36}$$

At the interfaces between MEM/CL and GDL/BP, a condition of zero flux was established for mass, momentum, species, and water. Nevertheless, at interfaces between MEM/CL, for the charge, heat, and water transport, and at interfaces between

GDL/BP, for heat transport and electronic phase, coupled boundary conditions were implemented. The anode terminal was maintained at a fixed voltage of zero, while the cathode terminal was set to operate at the established potential.

Table 3.3 Operational and Electrochemical Parameters [73]–[75], [88], [91], [98]

Parameters	Value	Units
OCV	1.10	V
Operating Temperature	343.15	K
Operating Pressure	1.0	atm
Anode Stoichiometric Ratio	2.0	-
Cathode Stoichiometric Ratio	3.0	-
Anode/Cathode Relative Humidity	100/100	%
Anode reference Current density	10000	A/cm^2
Anode reference Current density	10	A/cm^2
PEM equivalent weight	1.1	kg/mol
Anode/Cathode transfer coefficient	0.5/0.5	-
Reference concentration of H_2/O_2	56.4/3.39	mol/m^3
Density of MEM	1980.0	kg/m^3
Liquid water density	1000.0	kg/m^3
Thermal Conductivity of CL, GDL, MEM, BP	1.0, 1.7, 0.95, 20.0	W/mK
Electronic Conductivity of BP, GDL, CL	80000, 5000, 1000	S/m
The porosity of GDL, CL	0.6, 0.3	-
Permeability of GDL, MEM, CL	10^{-12}, 10^{-20}, 10^{-13},	m^2
Bulk Diffusivity of H_2, O_2 and water vapour	$9.73*10^{-5}$, $2.73*10^{-5}$, $2.33*10^{-5}$	m^2/s

3.6.2 Numerical Treatment

The complete set of partial differential equations that govern the PEMFC was solved through the use of computational fluid dynamics (CFD) code Ansys Fluent 2022 R1, with the aid of PEMFC add-on modules. In this study, the utilized code employs a double-precision scheme that applies the finite volume method (FVM) to discretize all the differential equations associated with continuity, momentum, species, energy, protonic potential, electrical potential, and water content. The SIMPLE algorithm was

used to control the velocity-pressure coupling in the momentum equation., while an interpolation function based on the second-order upwind method was utilized. The iteration residual for all solution variables was fixed at 10^{-6}, and appropriate under-relaxation factors were applied to each variable to achieve a steady convergence.

3.7 GRID INDEPENDENCE AND MODEL VALIDATION

The computing domain was discretized using the suitable meshing scheme, as depicted in Figures 3.4 and 3.5. The mesh was chosen based on a grid-independent examination. Five different grid numbers were used in the investigation at 0.5V to assess the grid independence such as 1,23,929, 2,43,689, 4,41,677, 7,99,377, and 11,01,739, as illustrated in Figure 3.6. The current density showed a variation of less than 0.5% for the mesh with 7,99,377 nodes as compared to the mesh with 11,01,739 nodes. Based on the trade-off between accuracy and computational cost, a mesh size of 7,99,377 nodes was chosen for the numerical simulation. In the entire domain, a structured hexahedron mesh was utilized.
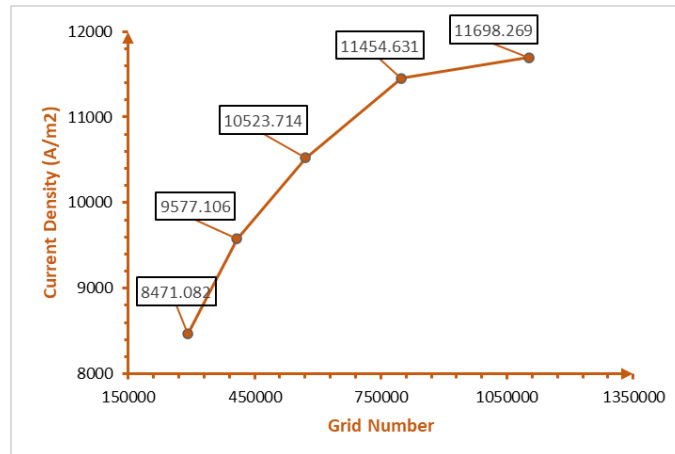

Figure 3.6: Mesh Independence Test at 0.5V

In order to demonstrate the accuracy of the fuel cell model developed in this study, a comparison was made between the simulated outcomes and the results obtained through experiment data provided by Wang et al.[99]**.** The results revealed a consistent decrease in current density as the cell voltage increased, as depicted in Figure 3.7. Throughout the entire range of current densities, the model's results aligned well with the experimental outcomes. However, a slight inconsistency was observed in the higher current density region. As a result, the numerical model envisaged in this study is feasible and realistic.
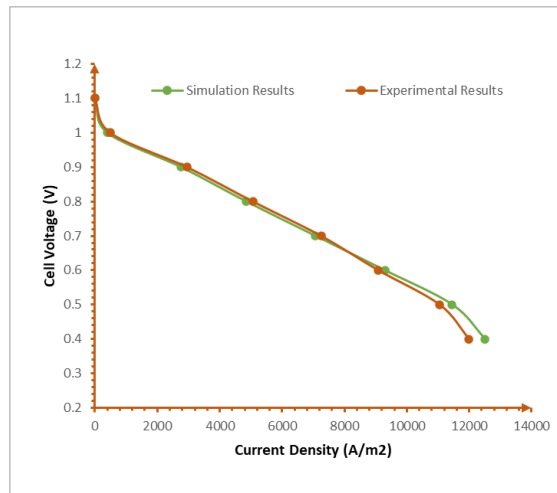
Figure 3.7: Comparison between the Polarization Curves of Simulation Results and Experimental Results

3.8 PARAMETERS SELECTION

Careful selection of appropriate parameters is crucial for studying the performance of PEMFCs, and the parameters were chosen with great caution. The following are the key parameters sought from the PEMFC:

- Current density
- Power density
- Pressure drop
- Temperature distribution
- Velocity distribution
- Reactant's concentration
- Water removal capability

CHAPTER 4

RESULTS AND DISCUSSION

4.1 INTRODUCTION

The key goal of this research is to create innovative tapered-trapezoidal FFDs that can enhance reactant distribution and water removal in PEMFCs. To achieve this, three novel tapered-trapezoidal FFDs were compared based on different parameters, specifically at an output voltage of 0.5V.

4.2 PERFORMANCE CURVES

The polarization and power density curves for all five cases are presented in Figures 4.1 and 4.2. Overall, the different FFDs exhibited similar behavior in terms of activation, ohmic, and concentration losses. However, the polarization curves for the parallel FFD followed a nearly logarithmic pattern, indicating that the primary factor influencing cell performance is the limitation of mass transport. This suggests that there is an insufficient amount of gases available for the reactions, leading to gas depletion in certain regions of the active area. As an outcome, the performance of the PEMFC is significantly reduced.
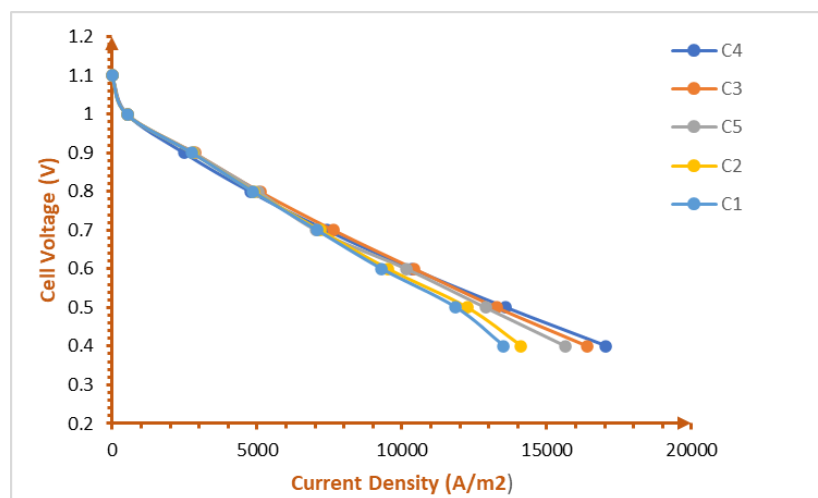

Figure 4.1: Polarization Curves for all the Five Cases

When the operating voltage exceeds 0.7V, specifically in the region of activation and ohmic losses, the polarization curves for the different FFDs coincide, indicating that the FFDs do not impact the performance of the PEMFC. When working at higher voltages, the rate of the electrochemical reaction is slower and oxygen utilization is limited, a small quantity of oxygen is adequate for the chemical reaction. This can be observed in Figure 1.4. The variation in reactant distribution does not affect the electrochemical reactions, as all five cases provide sufficient oxygen for these reactions. As a result, all the designs exhibit similar levels of performance.
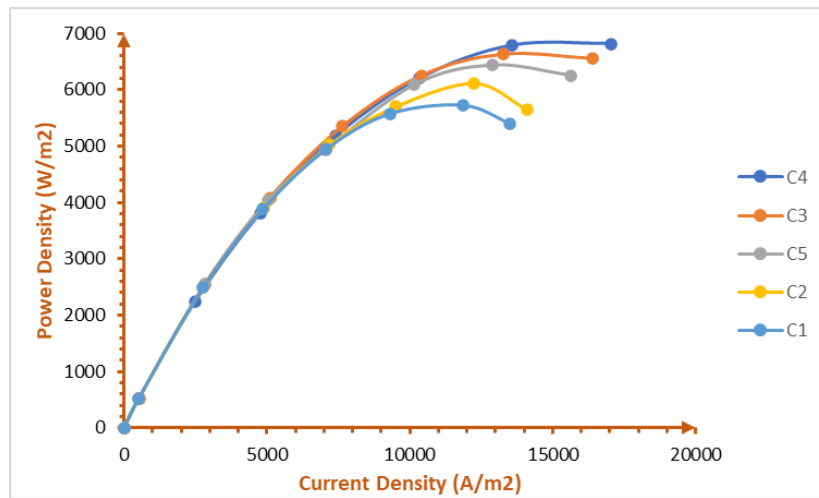

**Figure 4.2: Power Density Curves for All the Five Cases**

Nevertheless, as the operating voltage decreases, particularly in the region of concentration losses, the rate of electrochemical reactions increases along with oxygen consumption. Consequently, the FFD plays a substantial role in deciding the overall performance of the cell. The introduction of novel tapered-trapezoidal FFDs, with varying dimensions of "a" and "b" as depicted in Figure-3.2, yields notable distinctions in polarization and power density curves when compared to both the conventional straight parallel FFD and the tapered parallel FFD. It becomes evident that all the novel tapered-trapezoidal FFDs consistently enhance cell performance by facilitating improved reactant transport, which is attributed to increased contact areas between the channels and GDL at a lower operating potential.

It should be noted that the cell performance first increases for case C3(a=1.2; b=0.8) and C4 (a=1.4; b=0.6) and then decreases for case C5 (a=1.6; b=0.4) due to alterations in the amount of dissolved water content in the MEA. The trade-off between mass transport and water removal capability has been carefully considered to obtain the

optimal tapered-trapezoidal FFD. This indicates that the FFD significantly contributes to minimizing concentration losses, particularly at high current densities. A further observation of Figure 4.1 and 4.2 indicate that C4 (a=1.4; b=0.6) has the maximum cell performance among all five cases at 0.5 V, which improves the limiting current density and peak power density by 13.8 % and 8.1 % relative to the case C1, respectively and by 7.9 % and 4.3 % compared to C2 (tapered parallel FFD) respectively. The results here indicate that the proposed novel FFD has a positive effect on the operational efficiency, especially at lower cell voltage. However, the operational efficiency will be different with changes in dimensions of "a" and "b" (as shown in Figure-3.2). and the variation in the cell performance for all the cases is further explained in the following section.

4.3 TEMPERATURE DISTRIBUTION

The fuel cell only relies on convective heat transfer from the reaction gases for heat dissipation because the PEMFC model used in this study lacks a cooling channel. It is widely recognized that a higher temperature within the PEM in the PEMFC can aid in reducing voltage losses and ultimately result in improved cell performance. This relationship is demonstrated in Figure-4.3, which portrays the situation when the FC operates at an output voltage of 0.5V.

Figure-4.3: Static Temperature Distribution Profile within Membrane at 0.5 V
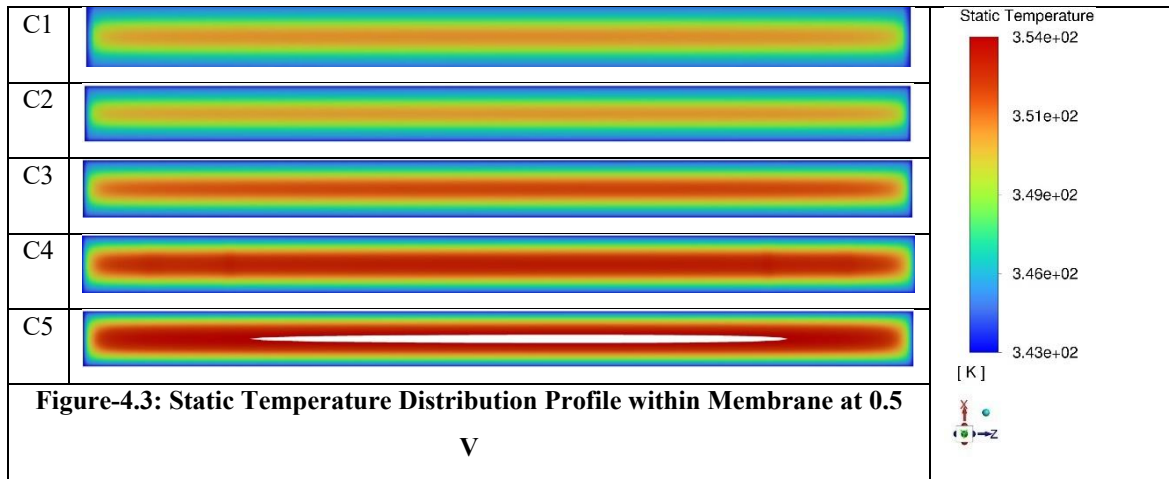
The temperature inside the membrane of C1 is lower than that of the C2, C3, C4, and C5. This is because the C1 has a reduced concentration of reactants which results in a weaker reaction and generates less heat. On the other hand, the C2, C3, C4, and C5 have a higher concentration of reactants, leading to an increase in the temperature inside the membrane as well as an increase in heat production respectively. The maximum

temperature inside all five cases of the PEMFC with different FFDs is 350.6 K, 351.9K, 352.4K, 353.3K, and 354.6 K respectively, resulting in a higher average temperature within the PEM as shown in Figure-4.4.
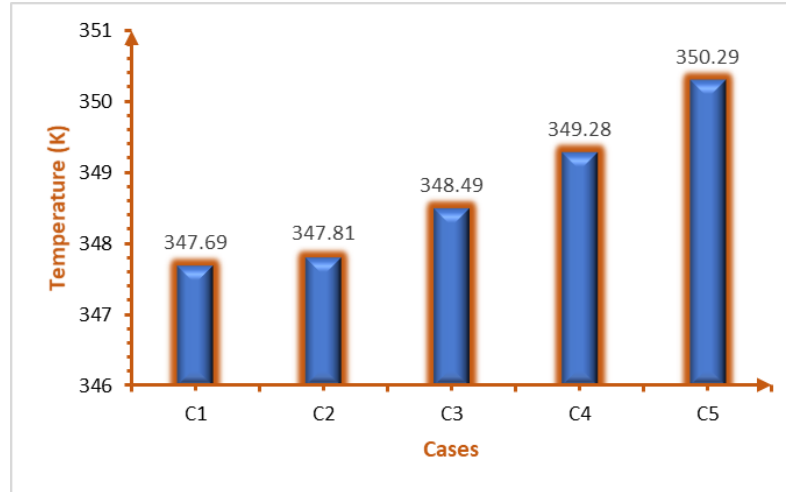

Figure-4.4: Average Temperature within Membrane at 0.5 V

The temperature distribution is a crucial parameter that impacts the performance of PEMFCs. This conveyance is connected with the electrochemical activities happening inside the energy unit. The MEA, which comprises the GDL, CL, and PEM, serves as the location for these reactions and involves intricate transport processes. A non-homogeneous temperature distribution or the presence of localized hotspots can cause thermal stress within the MEA, adversely affecting its service life. Figure 4.3 portrays the temperature variation in the z-direction within the MEA, highlighting temperature tops occurring in the middle of the PEM. By comparing all five cases, it is observed that the conventional FFDs in the PEMFC result in a non-homogeneous temperature variation in the z-direction because of excessive concentration losses. However, the novel tapered-trapezoidal FFDs effectively mitigate this issue by reducing concentration polarization and minimizing the rate of temperature drop. Nevertheless, C5 exhibits a less uniform temperature distribution compared to C3 and C4, which will be further explained in subsequent stages of the present study. Consequently, the novel tapered-trapezoidal FFDs C4 leads to a consistently uniform temperature variation within the MEA. As an outcome, these FFDs have the ability to enhance heat transfer effectiveness and significantly improve the homogeneity of temperature variation within the MEA, particularly in regions with high current density.

4.4 VELOCITY DISTRIBUTION

The reaction activities within the MEA are primarily influenced by the distribution of reactants, which is, in turn, heavily dependent on the fluid flow conditions within the PEMFC. Figure 4.5 shows the velocity profile on the x-z -plane at the interface of the cathode channel and the CGDL with an output voltage of 0.5 V.

Figure-4.5: Velocity Magnitude Profile at Cathode Channel and CGDL Interface at 0.5 V
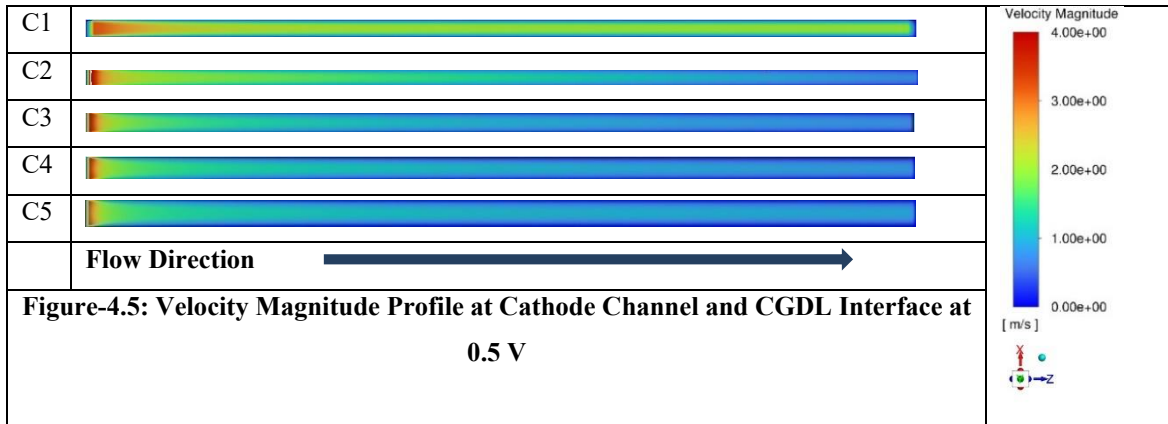
As the conventional FFD (C1) shows a higher velocity along the flow direction hence resulting in less diffusion of reactants into GDL and consequently low amount of oxygen takes part in the electrochemical reaction. It is obvious from Figure 4.5 demonstrates that the novel tapered-trapezoidal FFDs significantly slow the gas's velocity in the flow direction on the cathode side. Pressure changes in the flow channel as a result of the varying velocity in the z-direction cause a pressure gradient between the GDL and the flow channel. This pressure gradient facilitates the diffusion of fluid and promotes its transport. The enhancement of diffusive transport of the novel tapered-Trapezoidal FFD also yields an increase in under rib reactants concentration for C2, C3, C4, and C5 respectively with the reduction in average velocities along the flow direction at the interface between the GDL and the cathode channel as shown in Figure 4.6. From Figure 4.6 it is clear that the novel tapered-trapezoidal FFDs C5 results in the highest reduction in average velocity with 11.85 % as compared to the straight conventional FFD followed by C4, C3, and C2 with 10.48 %, 8.03 %, and 3.31 % respectively at 0.5 V. Consequently, this leads to improved uniformity of reactant gases within the GDLs, significantly influencing the mass transfer of reactants when implementing the suggested novel tapered-trapezoidal FFDs. As a result, the consumption of oxygen is more evenly distributed when the gas velocity on the cathode

side is decreased, resulting in a uniform distribution of current density. The discoveries of Zeroual et al. are consistent with this observation [100].
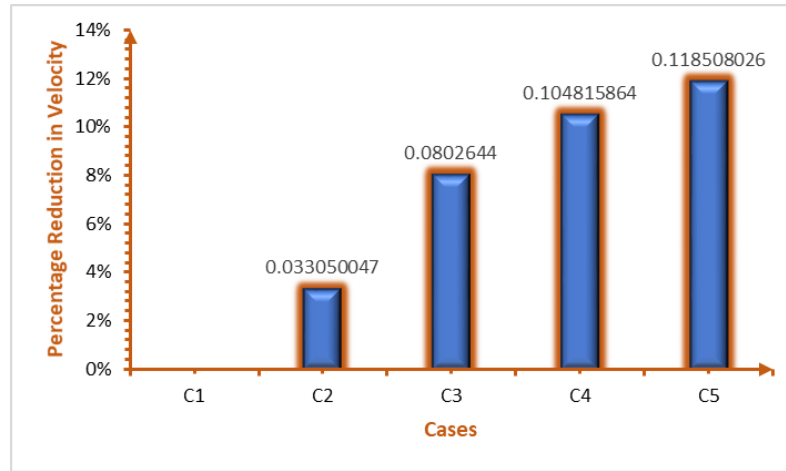

Figure-4.6: Reduction in Average Velocity Magnitude at Cathode Channel and CGDL Interface at 0.5 V

Therefore, the implementation of novel tapered-trapezoidal FFDs with wider and thinner ribs facilitates a more consistent consumption of reactants.
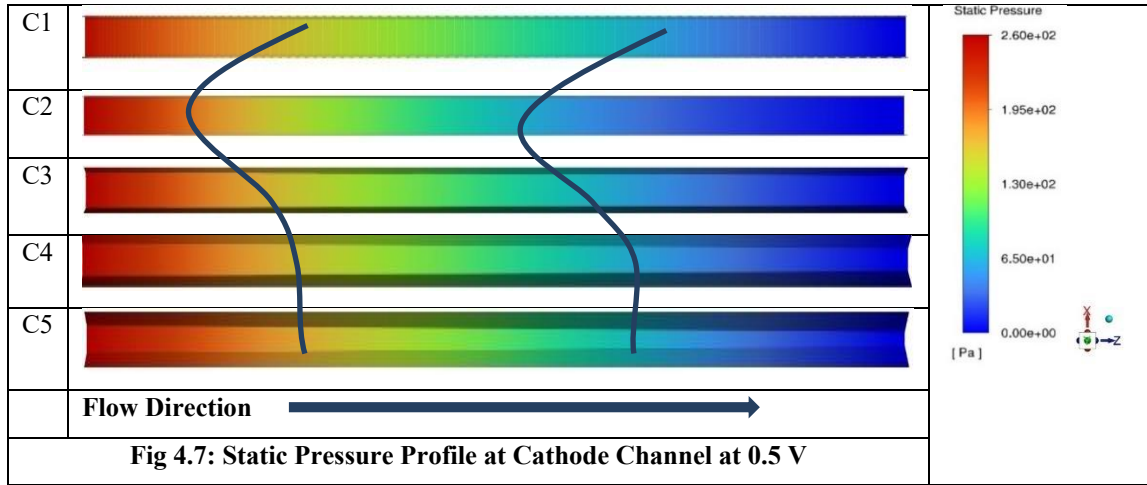
4.5 PRESSURE DROP

When designing FC, the flow channel's geometry is imperative in determining the pressure drop. By and large, the progressions in the cross-sectional shape significantly affect the pressure drop, which can be ascribed to the impact of the hydraulic diameter on the pressure drop. On account of a PEMFC with parallel through channels or serpentine channels, the pressure drops essentially result from the friction between the fluid and the channel. The friction that occurs between the fluid and the flow channel is the primary factor that contributes to pressure drop. The Darcy-Weisbach equation can be used to describe the frictional loss when the Reynolds number is less than 2000.

$$\Delta P_f = \frac{1}{2} f \Delta l \frac{\rho_g . u_g^2}{D_h} \qquad (4.1)$$

Where, ΔP_f represenets the friction loss; $f = \frac{64}{R_e}$: the coefficient of friction; Δl: the length in the section of developed flow; ρ_g and u_g: the density and velocity of reactant gas, respectively; D_h is the hydraulic diameter. Figure 4.7 illustrates the distribution of pressure along the flow direction within the cathode channel for all five cases at 0.5V. The pressure variation is a crucial parameter that directly or indirectly impacts the

reactions and electrical performance of the cell. Additionally, it interacts with other factors within the cell, including water control, further influencing overall performance.

Fig 4.7: Static Pressure Profile at Cathode Channel at 0.5 V

It is noticed that the conventional straight parallel FFD has less variation along the flow direction. Hence it results in less pressure drop along the flow direction as displayed in Figure 4.8. which also portrays that case C2 has the highest pressure drop among all the FFDs.
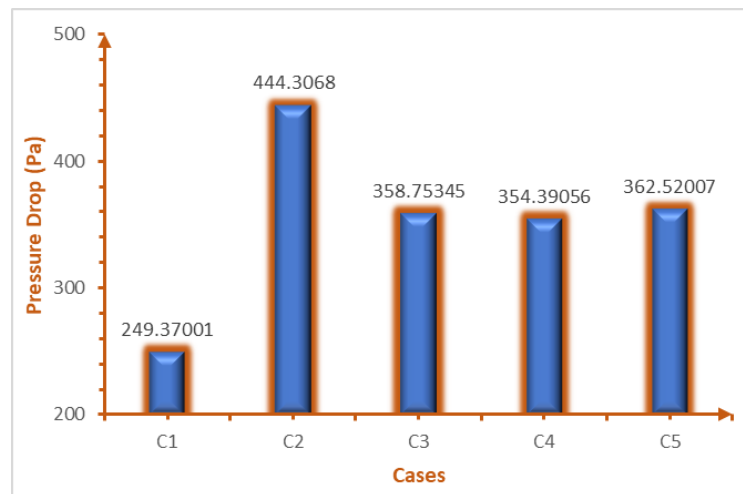
Figure-4.8: Pressure Drop within the Cathode Channel at 0.5 V

An increase in pressure drop necessitates additional power for pumping the reactants. Therefore, a better way to assess the performance of the FFD in PEMFCs is to measure the net power density, which is calculated by subtracting the cell power density from the parasitic power loss (pumping losses). As we can see from Figure 4.8 that the novel tapered-trapezoidal FFDs have more pressure drop as compared to C1 while less pressure drop as compared to C2. Hence, the novel tapered-trapezoidal FFDs will result in higher net power density as compared to C1 and C2. The pressure drop for C4 is

minimum among the tapered-trapezoidal FFDs, hence it results in the maximum net power density. Therefore, C4 gives maximum performance among all the FFDs.

4.6 REACTANTS CONCENTRATION FIELD

The reaction is started by the reactant gas entering the catalytic layer through the GDL from the flow channel. As a result, determining the channel's capacity to efficiently transfer reactant mass relies heavily on the mass fraction of the reactants present on the surface of the GDL. Figures 4.9 and 4.10 compare the distribution of reactants at the interface between the GDL and the channel in each of the five cases at 0.5 V. Because, as the reactants are consumed through electrochemical reactions, their proportion tends to decrease as they move along the flow direction in FC.

Figure 4.9 Mass Fraction of H$_2$ at Channel and GDL interface of Anode Side at 0.5 V
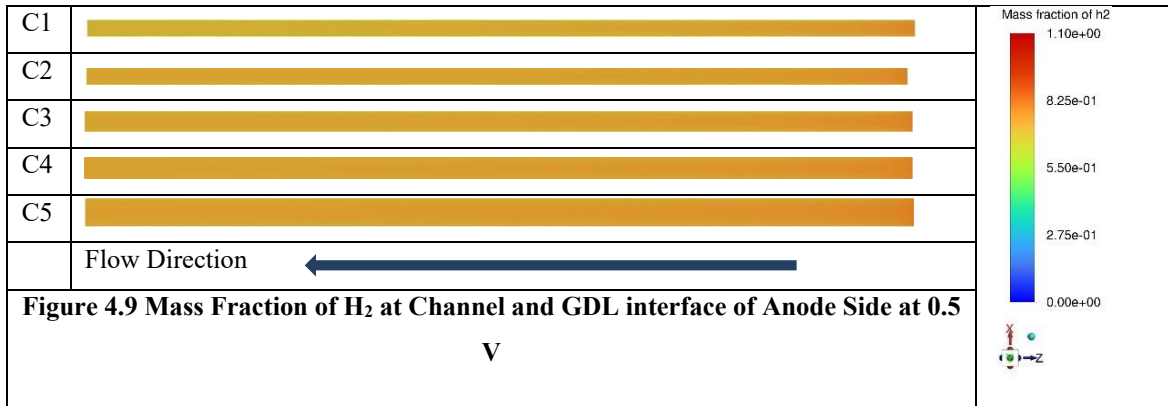
Figure 4.9 and Figure 4.10 demonstrated that the concentration of hydrogen exhibits a more consistent distribution compared to the concentration of oxygen at the interface between the channel and GDL in all scenarios. The primary reason behind the limited variation in hydrogen concentration is attributed to its higher diffusivity in comparison to oxygen.

Figure 4.10: Mass Fraction of O$_2$ at Channel and GDL Interface of Cathode Side at 0.5 V
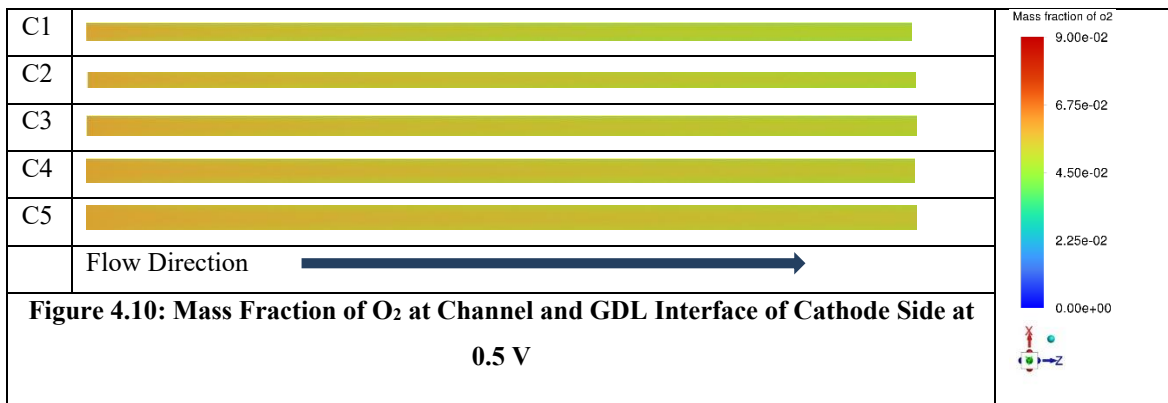
The use of novel tapered-trapezoidal FFDs in the anode side of FC led to a more uniform hydrogen concentration compared to the conventional FFD as shown in Figure 4.9. This is owing to the fact that the channel has a trapezoidal cross-section as well as the slope has a positive inclination along the course of the stream, which expands the contact region between the channel and the GDL. As a result, there is a higher diffusion of hydrogen towards the GDL, leading to a more uniform hydrogen distribution. The average hydrogen mass fraction at the interface between the channel and the GDL on the anode side is depicted in Figure 4.11 for each of the five scenarios. It demonstrates that the average hydrogen mass fraction is higher by approximately 2.0%, 3.5%, 4.0%, and 5% for the cases C2, C3, C4, and C5 respectively when compared to the conventional FFD.
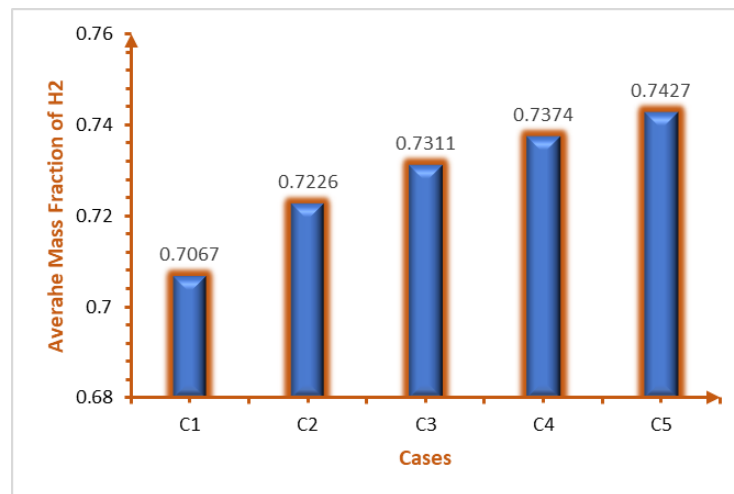
Figure 4.11: Average Mass Fraction of H₂ at Anode Channel and AGDL Interface at 0.5 V

Nevertheless, the primary electrochemical reaction predominantly occurs on the cathode side at the CL. This is where protons beginning from the anode side, alongside oxygen and electrons from the cathode side, consolidate and bring about the production of electrical current and water as a by-product. The novel tapered-trapezoidal FFDs, C3, C4, and C5 have a rising contact region between the channel and the GDL respectively. This facilitates easier movement of oxygen from the channel to the GDL, leading to more uniform diffusion within the GDL itself, as shown in Figure 4.10. Consequently, a larger number of reactants are able to actively engage in the reaction occurring in the CL. Ultimately, this improvement in reactant availability and distribution enhances the performance of the PEMFC. The mass fraction of oxygen diminishes steadily as the flow progresses, primarily due to the movement of oxygen from the flow channel to the GDL. Subsequently, oxygen diffuses from the GDL in both directions beneath the ribs

of the PEMFC and improves the homogeneity of the oxygen mass fraction in the whole active surface of the PEMFC.

The mean oxygen mass fraction at the interface of the channel (CH) and GDL is depicted in Figure 4.12. In comparison to Case C1, the mean mass fraction of oxygen in Cases 2, 3, 4, and 5 show an increase of 5.5%, 13.2%, 19.8%, and 21.6% respectively, specifically at 0.5 V.
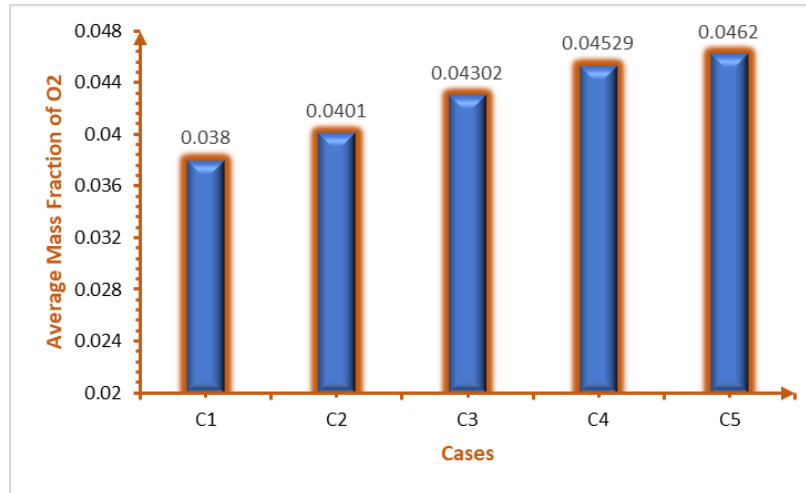
Figure 4.12: Average Mass Fraction of O$_2$ at Cathode Channel and CGDL Interface at 0.5 V

In conclusion, the use of tapered-trapezoidal flow field designs (FFDs) has an astounding impact on increasing the mass fraction of reactants that move into the GDL within the fuel cell. This, in turn, results in an improved uniformity in the distribution of reaction gases within the fuel cell. Ultimately, this enhanced distribution of reactants allows for a more efficient and effective electrochemical reaction, leading to a reduction in concentration overpotential.

4.7 WATER REMOVAL CAPABILITY

Investigating the concentration of water in the MEA will provide insight into the FFD's drainage capability. In PEMFCs, the CCL is primarily responsible for producing liquid water, which is ultimately evacuated from the cell utilizing an effective FFD. The presence of liquid water ensures that the membrane remains hydrated and makes it possible for protons to move. Nevertheless, the presence of water inside the cell hampers the operational efficiency of the PEMFC by blocking gas dissemination transmission, bringing about decreased dispersion rates and responsive regions. Subsequently, the performance of PEMFCs depends on keeping a decent water balance inside the cell, which can be disturbed by flooding or drying. It is necessary to note that

the FFD plays a dual role in facilitating reactant transfer and distribution, as well as managing water within the PEMFC. Both of these aspects significantly drive the performance of the PEMFC. As a consequence, this section investigates the crucial characteristics of the optimal channel for removing liquid water. At lower current density regions, the difference in water content at the membrane surface is not significant, and this time the novel tapered-trapezoidal FFDs have insignificant discharge advantage over the conventional straight FFD. However, when it comes to the conventional FFD, it faces difficulties in timely liquid water drainage from the CL via the flow channel and hence, low reactant distribution within the FC water, thereby increasing the likelihood of flooding.

At a cell potential of 0.5 V, the dissolved water content profiles within the membrane that follow the flow direction for various FFDs are depicted in Figure 4.13. Water is produced during the electrochemical reaction, which causes the water content to gradually increase in the flow direction as the reaction progresses. The average dissolved water content in the PEM decreases from 3.11 (C1) to 2.89 (C2), and further decreases to 2.80, 2.65, and 2.36 for the novel tapered FFDs; C3, C4, and C5 respectively.

Figure 4.13: Dissolved Water Content Profile at Interface between Membrane and CCL at 0.5 V
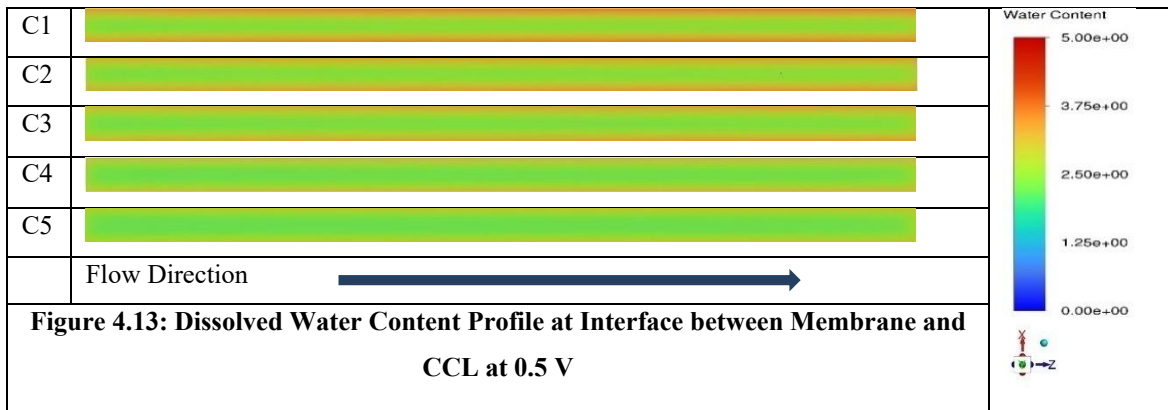
Furthermore, Figure 4.13 indicates that there is a steady increase in the dissolved liquid water content in the flow channel under the rib in the x-axis direction. This observation shows how liquid water behaves when it exits the cell through the flow channel. The novel tapered-trapezoidal FFDs namely; C3, C4, and C5 feature narrower ribs, resulting in a corresponding reduction in the liquid water content beneath the rib. Figure 4.14 shows the percentage increase of water content at the membrane in case C2, C3, C4, and C5 with respect to case C1. It is worth noting that the novel tapered-trapezoidal FFDs are expected to produce a larger amount of liquid water due to their

significantly higher current density at 0.5V. The novel tapered-trapezoidal FFDs have a wider bottom edge as well as a negative slope along the flow direction of the FFD which makes it simpler for the gas flow to eliminate the liquid water inside the PEMFC. This suggests that the novel tapered-trapezoidal FFDs exhibit a more effective capacity for liquid water removal.
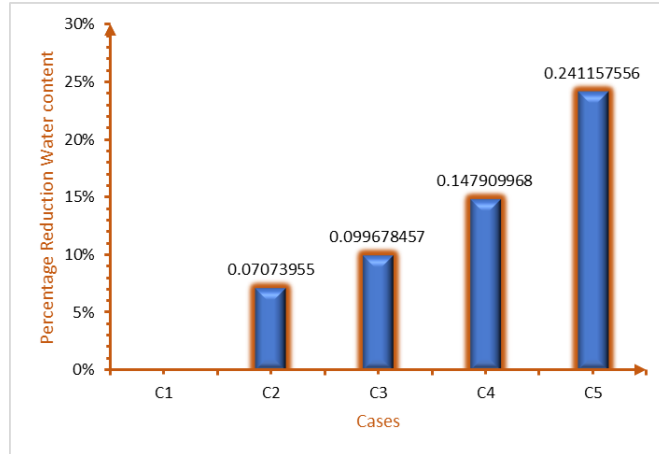

Figure 4.14: Percentage Reduction of Dissolve Water Content @ Interface between Membrane and CCL @ 0.5 V

This characteristic helps PEMFCs to manage water in an efficient manner and lower the likelihood of water flooding within the cell. However, it is important to note that, in comparison to cases C3 and C4, the novel trapezoidal FFD C5 has the lowest dissolved water content in the PEM among the various FFDs. As shown in Figure 4.3, the PEM's elevated temperature and remarkable capacity for water removal are the reasoning behind a very low percentage of liquid water within the MEA of case C5. Therefore, the novel-trapezoidal FFD C5 undoubtedly results in lesser cell performance than the novel-trapezoidal FFD C3 and C as shown in Figures 4.1 and 4.2, thus halting proton transport and weakening cell performance.

4.8 CURRENT DENSITY DISTRIBUTION

The variation in current density at the anode terminal when the operating voltage is 0.5V is depicted in Figure 4.15. It can be seen that the current density is lower under the channel than it is under the rib. The reason behind this is that the majority of electrons move through the ribs to the external circuit. At the channel intake, where the reactant concentration is highest, the highest current density is seen. Afterward, a decrease in the current density is observed along the flow direction. This is due to the decrease in the concentration of reactants along the flow direction as depicted in Figure

4.15. Insufficient reactant concentration can result in an uneven distribution of current density. At an operating cell potential of 0.5V, the current density variation of the novel tapered-trapezoidal FFD is more homogeneous compared to the conventional straight parallel FFD and tapered FFD. This superior consistency can be the result of the improved variation of reactants and temperature accomplished by the proposed novel FFDs, as previously examined.

Figure 4.15: Current Density Distribution at Anode Terminal at 0.5 V
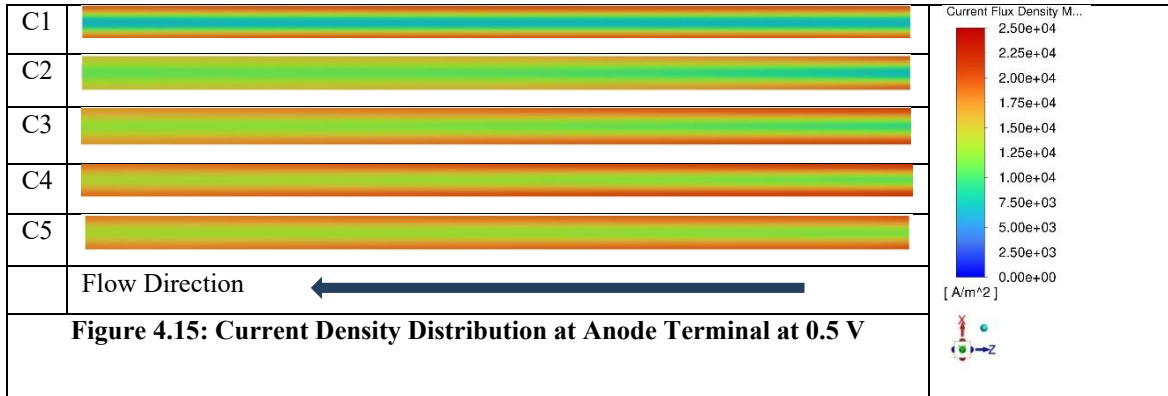
Figure 4.16 shows the average current densities at the anode terminal for all five cases at a cell potential of 0.5V.
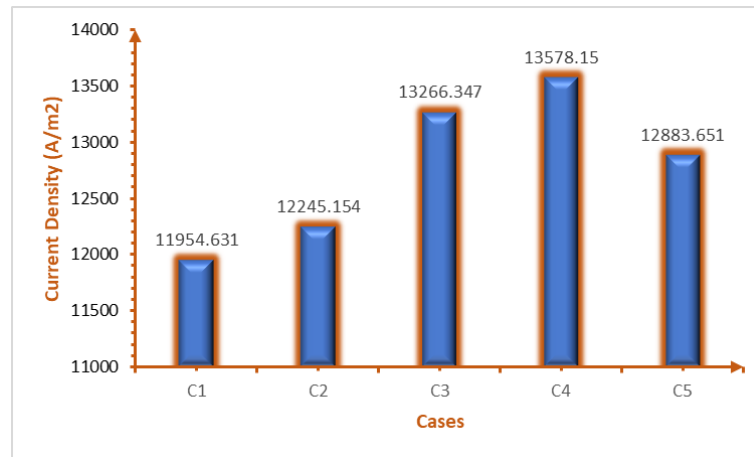
Figure 4.16: Average Current Density at Anode Terminal at 0.5 V

The average current densities of the tapered FFD; C2 and novel tapered-trapezoidal FFD; C3, C4, and C5 are 2.43 %, 10.97 %, 13.58 %, and 7.78 % more than that of the conventional straight parallel FFD respectively. However, C3 and C4 give 2.97 % and 5.39 % higher current density with respect to C5 respectively because C5 has the highest temperature at the membrane as compared to C3 and C4 which results in the dryness of the membrane and consequently yields lower current density compared to C3

and C4. Therefore, novel Tapered-trapezoidal FFD has a significant effect on the current density distribution as well as the average current density of the PEMFC.

CHAPTER 5

CONCLUSIONS AND SCOPE FOR FUTURE WORK

CONCLUSIONS

A three-dimensional (3D) computational fluid dynamics (CFD) model of the straight parallel FFD was utilized to investigate the impact of Flow field's geometric designs and dimensions on the performance and localized transport phenomena of PEMFCs. By numerical simulation, the present study proposed a novel tapered-trapezoidal FFD to investigate the mechanism by which it outperforms conventional straight parallel FFD and tapered FFD in PEMFC. The results were scrutinized within the scope of performance curves, temperature distributions, velocity distribution, pressure drop, reactant concentration field, water drainage capability, and current density distribution. The results indicate that the proposed novel tapered-trapezoidal FFDs perform better than the conventional as well as tapered parallel FFDs at low operating cell potential. However, at high operating cell potential, the novel tapered-trapezoidal FFDs have a very insignificant influence on the PEMFC operational efficiency and local species transport phenomena due to low reaction rates. Numerical results show that case C4 (a=1.4; b=0.6) improves the limiting current density by 13.8 % and 7.9 % as compared to cases C1 and C2 respectively and similarly the maximum power density of case C4 escalated by 8.1 % and 4.3 % as compared to the cases C1 and C2 respectively at 0.5 V. The results also describe that the temperature variation is more homogeneous in the MEA for the proposed FFDs as compared to the cases C1 and C2 and hence minimize the voltage losses at higher current density. Moreover, an increment in the average temperature of the proposed FFDs improves the heat transfer effectiveness of the PEMFC. However, case C5 results in the highest average temperature of 354.6 K and non-uniform temperature distribution as compared to cases C3 and C4. In addition, the reduction in velocity improves the diffusion of reactants, especially under the ribs in the channel, and boosted the reaction activity in the active area. The highest drop in pressure is observed in case of C2 among all cases, but its

performance is lower than the novel-trapezoidal FFDs. Such results indicate that a drop in pressure is not only the factor that enhances the performance. Nevertheless, case C4 has the minimum pressure drop among the proposed novel FFDs resulting in the maximum net power density. The enhancement of the reactant's variation and water drainage capability of the FFDs is crucial to improve the overall operational efficiency of PEMFC in high current density regions. The novel tapered-trapezoidal FFDs provided more homogeneous reactant distributions and current density than cases C1 and C2 due to the larger flow channel and GDL contact area. Also, due to the negative slope along the flow towards the cathode side in the proposed novel FFDs help in efficient water removal which is indicated by the low dissolved water content within the interface between the MEA and CCL. However, the high temperature and water removal capability of case C5 resulted in the dehydration of the MEA and hence lower its performance. In contrast to the conventional and tapered FFDs, the novel tapered-trapezoidal FFDs have more uniform temperature and reactants distributions, resulting in uniform current density and better performance in the cell.

Scope for future work

The output of the study has the potential to give an idea about the impact of FFDs in the PEMFC. As the global reliance on fossil fuels for energy production is well known, it is crucial to prioritize the efficiency of clean energy resources. Even a small improvement of 1% in the net power generated by fuel cells could have a significant impact, as it has the potential to reduce the consumption of substantial amounts of fossil fuels on a global scale. Due to these considerations, there is a need for further optimization in implementing the suggested tapered-trapezoidal flow field designs (FFDs) for PEMFCs. This optimization process should address two key aspects: firstly, the efficient manufacturing of the FFDs; and secondly, the development of a comprehensive design specifically tailored for their application in stacks.

REFERENCES

[1] "Allianz Risk Barometer 2023 - Energy crisis | AGCS." https://www.agcs.allianz.com/news-and-insights/expert-risk-articles/allianz-risk-barometer-2023-energy-crisis.html (accessed May 26, 2023).

[2] "World Energy Outlook 2022", Accessed: May 26, 2023. [Online]. Available: www.iea.org/t&c/

[3] I. - International Energy Agency, "Renewables 2022," 2022, Accessed: May 26, 2023. [Online]. Available: www.iea.org

[4] "The global energy crisis is ramping up interest in renewables, the IEA says | World Economic Forum." https://www.weforum.org/agenda/2023/01/renewables-energy-crisis-transition-iea (accessed May 26, 2023).

[5] I. Energy Agency, "India Energy Outlook 2021 World Energy Outlook Special Report", Accessed: May 26, 2023. [Online]. Available: www.iea.org/t&c/

[6] "Country insight – India | Energy economics | Home." https://www.bp.com/en/global/corporate/energy-economics/statistical-review-of-world-energy/country-and-regional-insights/india.html (accessed May 26, 2023).

[7] "Renewable Energy in India - Indian Power Industry Investment." https://www.investindia.gov.in/sector/renewable-energy (accessed May 26, 2023).

[8] "Press Information Bureau." https://pib.gov.in/FeaturesDeatils.aspx?NoteId=151141&ModuleId%20=%202 (accessed May 26, 2023).

[9] "Energy demand growth in India by scenario, 2019-2040 – Charts – Data & Statistics - IEA." https://www.iea.org/data-and-statistics/charts/energy-demand-growth-in-india-by-scenario-2019-2040 (accessed May 26, 2023).

[10] "Homepage | National Oceanic and Atmospheric Administration." https://www.noaa.gov/ (accessed May 26, 2023).

[11] "Projected CO2 emissions worldwide 2050 | Statista." https://www.statista.com/statistics/263980/forecast-of-global-carbon-dioxide-emissions/ (accessed May 26, 2023).

[12] "CO2 emissions - Our World in Data." https://ourworldindata.org/co2-emissions (accessed May 26, 2023).

[13] "All About Climate." https://education.nationalgeographic.org/resource/all-about-climate/ (accessed May 26, 2023).

[14] "Climate change." https://www.who.int/health-topics/climate-change#tab=tab_1 (accessed May 26, 2023).

[15] "Causes and Effects of Climate Change | United Nations." https://www.un.org/en/climatechange/science/causes-effects-climate-change (accessed May 26, 2023).

[16] "World | Total including LUCF | Greenhouse Gas (GHG) Emissions | Climate Watch." https://www.climatewatchdata.org/ghg-emissions?chartType=percentage&end_year=2019&start_year=1990 (accessed May 26, 2023).

[17] "Marking the Kyoto Protocol's 25th anniversary | United Nations." https://www.un.org/en/climatechange/marking-kyoto-protocol%E2%80%99s-25th-anniversary (accessed May 26, 2023).

[18] "India's renewable energy journey: Short-term hiccups but long-term trajectory intact | IEEFA." https://ieefa.org/resources/indias-renewable-energy-journey-short-term-hiccups-long-term-trajectory-intact?gclid=CjwKCAjwpayjBhAnEiwA-7ena9tzywCVYhh_fboaTQQ06iIxweFoUJocC1p4zH2jL8hP32fgCOW4nhoCSQUQAvD_BwE (accessed May 26, 2023).

[19] S. Chakraborty *et al.*, "A Review on the Numerical Studies on the Performance of Proton Exchange Membrane Fuel Cell (PEMFC) Flow Channel Designs for Automotive Applications," *Energies 2022, Vol. 15, Page 9520*, vol. 15, no. 24, p. 9520, Dec. 2022, doi: 10.3390/EN15249520.

[20] "Fuel Cells | Department of Energy." https://www.energy.gov/eere/fuelcells/fuel-cells (accessed May 26, 2023).

[21] W. R. G. Esq. M. A. M.R.I., "XLII. On a small voltaic battery of great energy; some observations on voltaic combinations and forms of arrangement; and on the inactivity of a copper positive electrode in nitro-sulphuric acid," *https://doi.org/10.1080/14786443908649881*, vol. 15, no. 96, pp. 287–293, Oct. 2009, doi: 10.1080/14786443908649881.

[22] W. R. G. Esq. M.A., "XXIV. On voltaic series and the combination of gases by platinum," *https://doi.org/10.1080/14786443908649684*, vol. 14, no. 86–87, pp. 127–130, Feb. 2009, doi: 10.1080/14786443908649684.

[23] B. Cook, "Introduction to fuel cells and hydrogen technology," *Engineering Science and Education Journal*, vol. 11, no. 6, pp. 205–216, 2002, doi: 10.1049/ESEJ:20020601.

[24] "V. A new form of gas battery," *Proceedings of the Royal Society of London*, vol. 46, no. 280–285, pp. 296–304, Dec. 1890, doi: 10.1098/RSPL.1889.0036.

[25] F. T. Bacon, "Fifth world hydrogen energy conference 15–19 July 1984 division D 'conversion and utilization'. The development and practical application of fuel cells: Keynote address," *Int J Hydrogen Energy*, vol. 10, no. 7–8, pp. 423–430, Jan. 1985, doi: 10.1016/0360-3199(85)90070-9.

[26] "Francis Thomas Bacon | British engineer | Britannica." https://www.britannica.com/biography/Francis-Thomas-Bacon (accessed May 26, 2023).

[27] P. Grimes, "Historical pathways for fuel cells. The new electric century," *Proceedings of the Annual Battery Conference on Applications and Advances*, vol. 2000-January, pp. 41–45, 2000, doi: 10.1109/BCAA.2000.838369.

[28] H. Mohammed, A. Al-Othman, P. Nancarrow, Y. Elsayed, and M. Tawalbeh, "Enhanced proton conduction in zirconium phosphate/ionic liquids materials for high-temperature fuel cells," *Int J Hydrogen Energy*, vol. 46, no. 6, pp. 4857–4869, Jan. 2021, doi: 10.1016/J.IJHYDENE.2019.09.118.

[29] P. Li *et al.*, "Exploring MnCr2O4–Gd0.1Ce0.9O2-δ as a composite electrode material for solid oxide fuel cell," *Int J Hydrogen Energy*, vol. 44, no. 59, pp. 31333–31341, Nov. 2019, doi: 10.1016/J.IJHYDENE.2019.09.196.

[30] R. J. Kee, P. Korada, K. Walters, and M. Pavol, "A generalized model of the flow distribution in channel networks of planar fuel cells," *J Power Sources*, vol. 109, no. 1, pp. 148–159, Jun. 2002, doi: 10.1016/S0378-7753(02)00090-3.

[31] W. Qi *et al.*, "Mechanisms insight into oxygen reduction reaction on sulfur-doped Fe–N2 graphene electrocatalysts," *Int J Hydrogen Energy*, vol. 45, no. 1, pp. 521–530, Jan. 2020, doi: 10.1016/J.IJHYDENE.2019.10.205.

[32] E. Asadian, S. Shahrokhian, and A. Iraji Zad, "ZIF-8/PEDOT @ flexible carbon cloth electrode as highly efficient electrocatalyst for oxygen reduction reaction," *Int J Hydrogen Energy*, vol. 45, no. 3, pp. 1890–1900, Jan. 2020, doi: 10.1016/J.IJHYDENE.2019.11.124.

[33] N. Matulić, G. Radica, F. Barbir, and S. Nižetić, "Commercial vehicle auxiliary loads powered by PEM fuel cell," *Int J Hydrogen Energy*, vol. 44, no. 20, pp. 10082–10090, Apr. 2019, doi: 10.1016/J.IJHYDENE.2018.12.121.

[34] H. Ito, "Economic and environmental assessment of phosphoric acid fuel cell-based combined heat and power system for an apartment complex," *Int J Hydrogen Energy*, vol. 42, no. 23, pp. 15449–15463, Jun. 2017, doi: 10.1016/J.IJHYDENE.2017.05.038.

[35] A. C. Turkmen, C. Celik, and H. Esen, "The statistical relationship between flow channel geometry and pressure drop in a direct methanol fuel cell with parallel channels," *Int J Hydrogen Energy*, vol. 44, no. 34, pp. 18939–18950, Jul. 2019, doi: 10.1016/J.IJHYDENE.2019.04.034.

[36] J. Milewski, K. Futyma, and A. Szczęśniak, "Molten carbonate fuel cell operation under high concentrations of SO2 on the cathode side," *Int J Hydrogen Energy*, vol. 41, no. 41, pp. 18769–18777, Nov. 2016, doi: 10.1016/J.IJHYDENE.2016.03.121.

[37] R. Dawson, A. Patel, K. Alako, S. Parhar, C. Hinde, and C. Reynolds, "In-operando optical observations of alkaline fuel cell electrode surfaces during harsh cycling tests," *Int J Hydrogen Energy*, vol. 42, no. 33, pp. 21203–21214, Aug. 2017, doi: 10.1016/J.IJHYDENE.2017.07.018.

[38] Y. Wang, D. Y. C. Leung, J. Xuan, and H. Wang, "A review on unitized regenerative fuel cell technologies, part B: Unitized regenerative alkaline fuel cell, solid oxide fuel cell, and microfluidic fuel cell," *Renewable and Sustainable*

Energy Reviews, vol. 75, pp. 775–795, Aug. 2017, doi: 10.1016/J.RSER.2016.11.054.

[39] L. Shu, J. Sunarso, S. S. Hashim, J. Mao, W. Zhou, and F. Liang, "Advanced perovskite anodes for solid oxide fuel cells: A review," *Int J Hydrogen Energy*, vol. 44, no. 59, pp. 31275–31304, Nov. 2019, doi: 10.1016/J.IJHYDENE.2019.09.220.

[40] "Fuel cell and its applications - energypedia." https://energypedia.info/wiki/Fuel_cell_and_its_applications (accessed May 26, 2023).

[41] S. Cheng, H. Liu, and B. E. Logan, "Power densities using different cathode catalysts (Pt and CoTMPP) and polymer binders (Nafion and PTFE) in single chamber microbial fuel cells," *Environ Sci Technol*, vol. 40, no. 1, pp. 364–369, Jan. 2006, doi: 10.1021/ES0512071/SUPPL_FILE/ES0512071SI20051017_095052.PDF.

[42] T. Sutharssan, D. Montalvao, Y. K. Chen, W. C. Wang, C. Pisac, and H. Elemara, "A review on prognostics and health monitoring of proton exchange membrane fuel cell," *Renewable and Sustainable Energy Reviews*, vol. 75, pp. 440–450, Aug. 2017, doi: 10.1016/J.RSER.2016.11.009.

[43] M. Mortada, H. S. Ramadan, J. Faraj, A. Faraj, H. El Hage, and M. Khaled, "Impacts of reactant flow nonuniformity on fuel cell performance and scaling-up: Comprehensive review, critical analysis and potential recommendations," *Int J Hydrogen Energy*, vol. 46, no. 63, pp. 32161–32191, Sep. 2021, doi: 10.1016/J.IJHYDENE.2020.06.013.

[44] M. Hu and G. Cao, "Research on the performance differences between a standard PEMFC single cell and transparent PEMFC single cells using optimized transparent flow field unit–Part I: Design optimization of a transparent flow field unit," *Int J Hydrogen Energy*, vol. 41, no. 4, pp. 2955–2966, Jan. 2016, doi: 10.1016/J.IJHYDENE.2015.12.144.

[45] Z. Xia, H. Chen, W. Shan, R. Zhang, T. Zhang, and P. Pei, "Behavior of current distribution evolution under reactant starvation conditions based on a single polymer electrolyte membrane fuel cell (PEMFC) with triple-serpentine flow field: An experimental study," *Int J Hydrogen Energy*, vol. 48, no. 36, pp. 13650–13668, Apr. 2023, doi: 10.1016/J.IJHYDENE.2022.12.187.

[46] Q. Tan, H. Lei, and Z. Liu, "Numerical simulation analysis of the performance on the PEMFC with a new flow field designed based on constructal-theory," *Int J Hydrogen Energy*, vol. 47, no. 23, pp. 11975–11990, Mar. 2022, doi: 10.1016/J.IJHYDENE.2022.01.243.

[47] C. Yang *et al.*, "Geometry optimization of a novel M-like flow field in a proton exchange membrane fuel cell," *Energy Convers Manag*, vol. 228, p. 113651, Jan. 2021, doi: 10.1016/J.ENCONMAN.2020.113651.

[48] Y. Li, Z. Zhou, X. Liu, and W. T. Wu, "Modeling of PEM fuel cell with thin MEA under low humidity operating condition," *Appl Energy*, vol. 242, pp. 1513–1527, May 2019, doi: 10.1016/J.APENERGY.2019.03.189.

[49] L. Jin, X. J. Wang, J. W. Zhu, C. F. Wang, T. T. Zhou, and X. W. Zhang, "Sensitivity analysis of proton exchange membrane fuel cell performance to operating parameters and its applicability assessment under different conditions," *Energy Convers Manag*, vol. 228, p. 113727, Jan. 2021, doi: 10.1016/J.ENCONMAN.2020.113727.

[50] R. Behrou, A. Pizzolato, and A. Forner-Cuenca, "Topology optimization as a powerful tool to design advanced PEMFCs flow fields," *Int J Heat Mass Transf*, vol. 135, pp. 72–92, Jun. 2019, doi: 10.1016/J.IJHEATMASSTRANSFER.2019.01.050.

[51] Q. Guo, J. Zheng, and Y. Qin, "Optimization of block structure parameters of PEMFC novel block channels using artificial neural network," *Int J Hydrogen Energy*, vol. 47, no. 90, pp. 38386–38394, Nov. 2022, doi: 10.1016/J.IJHYDENE.2022.09.017.

[52] Y. Leng, P. Ming, D. Yang, and C. Zhang, "Stainless steel bipolar plates for proton exchange membrane fuel cells: Materials, flow channel design and forming processes," *J Power Sources*, vol. 451, p. 227783, Mar. 2020, doi: 10.1016/J.JPOWSOUR.2020.227783.

[53] M. Marappan *et al.*, "Performance Studies of Proton Exchange Membrane Fuel Cells with Different Flow Field Designs – Review," *Chemical Record*, vol. 21, no. 4, pp. 663–714, Apr. 2021, doi: 10.1002/TCR.202000138.

[54] X. Li and I. Sabir, "Review of bipolar plates in PEM fuel cells: Flow-field designs," *Int J Hydrogen Energy*, vol. 30, no. 4, pp. 359–371, Mar. 2005, doi: 10.1016/J.IJHYDENE.2004.09.019.

[55] Y. Vazifeshenas, K. Sedighi, and M. Shakeri, "Numerical investigation of a novel compound flow-field for PEMFC performance improvement," *Int J Hydrogen Energy*, vol. 40, no. 43, pp. 15032–15039, Nov. 2015, doi: 10.1016/J.IJHYDENE.2015.08.077.

[56] L. S. Freire, E. Antolini, M. Linardi, E. I. Santiago, and R. R. Passos, "Influence of operational parameters on the performance of PEMFCs with serpentine flow field channels having different (rectangular and trapezoidal) cross-section shape," *Int J Hydrogen Energy*, vol. 39, no. 23, pp. 12052–12060, Aug. 2014, doi: 10.1016/J.IJHYDENE.2014.06.041.

[57] N. J. Cooper, T. Smith, A. D. Santamaria, and J. W. Park, "Experimental optimization of parallel and interdigitated PEMFC flow-field channel geometry," *Int J Hydrogen Energy*, vol. 41, no. 2, pp. 1213–1223, Jan. 2016, doi: 10.1016/J.IJHYDENE.2015.11.153.

[58] A. Hamrang, M. Abdollahzadeh, A. M. Bilondi, F. Bagherighajari, S. M. Rahgoshay, and J. C. Pascoa, "Comparison of PEMFC performance with parallel serpentine and parallel serpentine-baffled flow fields under various operating and geometrical conditions; a parametric study," *Int J Hydrogen Energy*, vol. 48, no. 20, pp. 7442–7459, Mar. 2023, doi: 10.1016/J.IJHYDENE.2022.11.122.

[59] W. Z. Li, W. W. Yang, N. Wang, Y. H. Jiao, Y. Yang, and Z. G. Qu, "Optimization of blocked channel design for a proton exchange membrane fuel

cell by coupled genetic algorithm and three-dimensional CFD modeling," *Int J Hydrogen Energy*, vol. 45, no. 35, pp. 17759–17770, Jul. 2020, doi: 10.1016/J.IJHYDENE.2020.04.166.

[60] F. Gong, X. Yang, X. Zhang, Z. Mao, W. Gao, and C. Wang, "The study of Tesla valve flow field on the net power of proton exchange membrane fuel cell," *Appl Energy*, vol. 329, p. 120276, Jan. 2023, doi: 10.1016/J.APENERGY.2022.120276.

[61] P. Lin, H. Wang, G. Wang, J. Li, and J. Sun, "Numerical study of optimized three-dimension novel Key-shaped flow field design for proton exchange membrane fuel cell," *Int J Hydrogen Energy*, vol. 47, no. 8, pp. 5541–5552, Jan. 2022, doi: 10.1016/J.IJHYDENE.2021.11.170.

[62] C. Yang *et al.*, "Geometry optimization of a novel M-like flow field in a proton exchange membrane fuel cell," *Energy Convers Manag*, vol. 228, p. 113651, Jan. 2021, doi: 10.1016/J.ENCONMAN.2020.113651.

[63] D. K. Dang and B. Zhou, "Effects of pin shapes on gas-liquid transport behaviors in PEMFC cathode," *J Power Sources*, vol. 557, p. 232584, Feb. 2023, doi: 10.1016/J.JPOWSOUR.2022.232584.

[64] M. Tamerabet, B. M. Hocine, S. Youcef, and M. Abdallah, "Unsteady three-dimensional numerical study of mass transfer in PEM fuel cell with spiral flow field," *Int J Hydrogen Energy*, vol. 42, no. 2, pp. 1237–1251, Jan. 2017, doi: 10.1016/J.IJHYDENE.2016.12.084.

[65] C. Suárez, A. Iranzo, B. Toharias, and F. Rosa, "Experimental and numerical Investigation on the design of a bioinspired PEM fuel cell," *Energy*, vol. 257, p. 124799, Oct. 2022, doi: 10.1016/J.ENERGY.2022.124799.

[66] D. K. Dang and B. Zhou, "Liquid water transport in PEMFC cathode with symmetrical biomimetic flow field design based on Murray's law," *Int J Hydrogen Energy*, vol. 46, no. 40, pp. 21059–21074, Jun. 2021, doi: 10.1016/J.IJHYDENE.2021.03.161.

[67] C. E. Damian-Ascencio, A. Saldaña-Robles, A. Hernandez-Guerrero, and S. Cano-Andrade, "Numerical modeling of a proton exchange membrane fuel cell with tree-like flow field channels based on an entropy generation analysis," *Energy*, vol. 133, pp. 306–316, Aug. 2017, doi: 10.1016/J.ENERGY.2017.05.139.

[68] B. Ramos-Alvarado, A. Hernandez-Guerrero, F. Elizalde-Blancas, and M. W. Ellis, "Constructal flow distributor as a bipolar plate for proton exchange membrane fuel cells," *Int J Hydrogen Energy*, vol. 36, no. 20, pp. 12965–12976, Oct. 2011, doi: 10.1016/J.IJHYDENE.2011.07.017.

[69] K. Tüber, A. Oedegaard, M. Hermann, and C. Hebling, "Investigation of fractal flow-fields in portable proton exchange membrane and direct methanol fuel cells," *J Power Sources*, vol. 131, no. 1–2, pp. 175–181, May 2004, doi: 10.1016/J.JPOWSOUR.2003.11.078.

[70] Y. Huang *et al.*, "Numerical investigation of baffle shape effects on performance and mass transfer of proton exchange membrane fuel cell," *Energy*, vol. 266, p. 126448, Mar. 2023, doi: 10.1016/J.ENERGY.2022.126448.

[71] Q. Zuo *et al.*, "Optimization of blocked flow field performance of proton exchange membrane fuel cell with auxiliary channels," *Int J Hydrogen Energy*, vol. 47, no. 94, pp. 39943–39960, Dec. 2022, doi: 10.1016/J.IJHYDENE.2022.09.143.

[72] Z. Zhang, F. Bai, P. He, Z. Li, and W. Q. Tao, "A novel cathode flow field for PEMFC and its performance analysis," *Int J Hydrogen Energy*, Apr. 2023, doi: 10.1016/J.IJHYDENE.2023.03.130.

[73] X. Chen *et al.*, "Performance study on a stepped flow field design for bipolar plate in PEMFC," *Energy Reports*, vol. 7, pp. 336–347, Nov. 2021, doi: 10.1016/J.EGYR.2021.01.003.

[74] M. Karimi Pashaki and J. Mahmoudimehr, "Performance superiority of an arc-shaped polymer electrolyte membrane fuel cell over a straight one," *Int J Hydrogen Energy*, vol. 48, no. 36, pp. 13633–13649, Apr. 2023, doi: 10.1016/J.IJHYDENE.2022.12.261.

[75] Y. Wang, X. Wang, Y. Fan, W. He, J. Guan, and X. Wang, "Numerical Investigation of Tapered Flow Field Configurations for Enhanced Polymer Electrolyte Membrane Fuel Cell Performance," *Appl Energy*, vol. 306, p. 118021, Jan. 2022, doi: 10.1016/J.APENERGY.2021.118021.

[76] Z. Chen, X. Yang, X. Hu, and C. Wang, "Optimization of channel structure for proton exchange membrane fuel cells based on a three-dimensional two-phase flow model," *Int J Energy Res*, vol. 45, no. 6, pp. 8794–8809, May 2021, doi: 10.1002/ER.6415.

[77] S. Mazumder and J. V. Cole, "Rigorous 3-D Mathematical Modeling of PEM Fuel Cells: I. Model Predictions without Liquid Water Transport," *J Electrochem Soc*, vol. 150, no. 11, p. A1503, Sep. 2003, doi: 10.1149/1.1615608.

[78] U. Pasaogullari and C.-Y. Wang, "Two-Phase Modeling and Flooding Prediction of Polymer Electrolyte Fuel Cells," 2005, doi: 10.1149/1.1850339.

[79] C. Spiegel, "PEM Fuel Cell Modeling and Simulation Using Matlab," *PEM Fuel Cell Modeling and Simulation Using Matlab*, pp. 1–443, Jan. 2008, doi: 10.1016/B978-0-12-374259-9.X5001-0.

[80] A. Albarbar and M. Alrweq, *Proton exchange membrane fuel cells: Design, modelling and performance assessment techniques*. Springer International Publishing, 2017. doi: 10.1007/978-3-319-70727-3.

[81] X. D. Niu, T. Munekata, S. A. Hyodo, and K. Suga, "An investigation of water-gas transport processes in the gas-diffusion-layer of a PEM fuel cell by a multiphase multiple-relaxation-time lattice Boltzmann model," *J Power Sources*, vol. 172, no. 2, pp. 542–552, Oct. 2007, doi: 10.1016/J.JPOWSOUR.2007.05.081.

[82]   J. M. Spurgeon, M. G. Walter, J. Zhou, P. A. Kohl, and N. S. Lewis, "Electrical conductivity, ionic conductivity, optical absorption, and gas separation properties of ionically conductive polymer membranes embedded with Si microwire arrays," *Energy Environ Sci*, vol. 4, no. 5, pp. 1772–1780, Apr. 2011, doi: 10.1039/C1EE01028J.

[83]   G. J. Offer, J. Mermelstein, E. Brightman, and N. P. Brandon, "Thermodynamics and kinetics of the interaction of carbon and sulfur with solid oxide fuel cell anodes," *Journal of the American Ceramic Society*, vol. 92, no. 4, pp. 763–780, Apr. 2009, doi: 10.1111/J.1551-2916.2009.02980.X.

[84]   Y. Zhou, B. Chen, W. Chen, Q. Deng, J. Shen, and Z. Tu, "A novel opposite sinusoidal wave flow channel for performance enhancement of proton exchange membrane fuel cell," *Energy*, vol. 261, p. 125383, Dec. 2022, doi: 10.1016/J.ENERGY.2022.125383.

[85]   X. Chen *et al.*, "Performance study on a stepped flow field design for bipolar plate in PEMFC," *Energy Reports*, vol. 7, pp. 336–347, Nov. 2021, doi: 10.1016/J.EGYR.2021.01.003.

[86]   J. Mahmoudimehr and A. Darbandi, "Technical study of a PEM fuel cell on the Psychrometric chart," *Int J Hydrogen Energy*, vol. 41, no. 1, pp. 607–613, Jan. 2016, doi: 10.1016/J.IJHYDENE.2015.10.123.

[87]   M. H. Akbari and B. Rismanchi, "Numerical investigation of flow field configuration and contact resistance for PEM fuel cell performance," *Renew Energy*, vol. 33, no. 8, pp. 1775–1783, Aug. 2008, doi: 10.1016/J.RENENE.2007.10.009.

[88]   M. Bilgili, M. Bosomoiu, and G. Tsotridis, "Gas flow field with obstacles for PEM fuel cells at different operating conditions," *Int J Hydrogen Energy*, vol. 40, no. 5, pp. 2303–2311, Feb. 2015, doi: 10.1016/J.IJHYDENE.2014.11.139.

[89]   J. H. Zhang, L. Bin Lei, D. Liu, F. Y. Zhao, F. Chen, and H. Q. Wang, "Numerical investigation of solid oxide electrolysis cells for hydrogen production applied with different continuity expressions," *Energy Convers Manag*, vol. 149, pp. 646–659, Oct. 2017, doi: 10.1016/J.ENCONMAN.2017.07.013.

[90]   X. Zeng, Y. Ge, J. Shen, L. Zeng, Z. Liu, and W. Liu, "The optimization of channels for a proton exchange membrane fuel cell applying genetic algorithm," *Int J Heat Mass Transf*, vol. 105, pp. 81–89, Feb. 2017, doi: 10.1016/J.IJHEATMASSTRANSFER.2016.09.068.

[91]   I. Chang *et al.*, "Performance enhancement in bendable fuel cell using highly conductive Ag nanowires," *Int J Hydrogen Energy*, vol. 39, no. 14, pp. 7422–7427, May 2014, doi: 10.1016/J.IJHYDENE.2014.03.017.

[92]   Y. Zhou *et al.*, "Optimization and evaluation criteria of water-gas transport performance in wave flow channel for proton exchange membrane fuel cell," *Int J Hydrogen Energy*, Mar. 2023, doi: 10.1016/J.IJHYDENE.2023.03.017.

[93] G. H. Guvelioglu and H. G. Stenger, "Computational fluid dynamics modeling of polymer electrolyte membrane fuel cells," *J Power Sources*, vol. 147, no. 1–2, pp. 95–106, Sep. 2005, doi: 10.1016/J.JPOWSOUR.2005.01.011.

[94] J. K. Kuo, T. H. Yen, and C. K. Chen, "Three-dimensional numerical analysis of PEM fuel cells with straight and wave-like gas flow fields channels," *J Power Sources*, vol. 177, no. 1, pp. 96–103, Feb. 2008, doi: 10.1016/J.JPOWSOUR.2007.11.065.

[95] T. E. Springer, T. A. Zawodzinski, and S. Gottesfeld, "Polymer Electrolyte Fuel Cell Model," *J Electrochem Soc*, vol. 138, no. 8, pp. 2334–2342, Aug. 1991, doi: 10.1149/1.2085971/XML.

[96] F. K. Hsu, M. S. Lee, C. C. Lin, Y. K. Lin, and W. T. Hsu, "A flexible portable proton exchange membrane fuel cell," *J Power Sources*, vol. 219, pp. 180–187, Dec. 2012, doi: 10.1016/J.JPOWSOUR.2012.07.054.

[97] J. Scholta, G. Escher, W. Zhang, L. Küppers, L. Jörissen, and W. Lehnert, "Investigation on the influence of channel geometries on PEMFC performance," *J Power Sources*, vol. 155, no. 1, pp. 66–71, Apr. 2006, doi: 10.1016/J.JPOWSOUR.2005.05.099.

[98] J. Hao, J. Chen, T. Ma, T. Hao, J. Zhou, and X. Du, "Flow channel structure optimization and analysis of proton exchange membrane fuel cell based on the finite data mapping and multi-field synergy principle," *Int J Heat Mass Transf*, vol. 207, p. 123997, Jun. 2023, doi: 10.1016/J.IJHEATMASSTRANSFER.2023.123997.

[99] L. Wang, A. Husar, T. Zhou, and H. Liu, "A parametric study of PEM fuel cell performances," *Int J Hydrogen Energy*, vol. 28, no. 11, pp. 1263–1272, Nov. 2003, doi: 10.1016/S0360-3199(02)00284-7.

[100] M. Zeroual, H. Ben Moussa, and M. Tamerabet, "Effect of Gas Flow Velocity in the Channels of Consumption Reactants in a Fuel Cell Type (PEMFC)," *Energy Procedia*, vol. 18, pp. 317–326, Jan. 2012, doi: 10.1016/J.EGYPRO.2012.05.043.